

# Massive galaxies in cosmological simulations: UV-selected sample at redshift $z = 2$

Kentaro Nagamine<sup>1</sup>, Renyue Cen<sup>2</sup>, Lars Hernquist<sup>1</sup>, Jeremiah P. Ostriker<sup>2,3</sup>,  
& Volker Springel<sup>4</sup>

## ABSTRACT

We study the properties of galaxies at redshift  $z = 2$  in a  $\Lambda$  cold dark matter ( $\Lambda$ CDM) universe, using two different types of hydrodynamic simulation methods – Eulerian TVD and smoothed particle hydrodynamics (SPH) – and a spectrophotometric analysis in the  $U_n, G, R$  filter set. The simulated galaxies at  $z = 2$  satisfy the color-selection criteria proposed by Adelberger et al. (2004) and Steidel et al. (2004) when we assume Calzetti extinction with  $E(B - V) = 0.15$ . We find that the number density of simulated galaxies brighter than  $R < 25.5$  at  $z = 2$  is about  $2 \times 10^{-2} h^3 \text{ Mpc}^{-3}$  for  $E(B - V) = 0.15$  in our most representative run, roughly one order of magnitude larger than that of Lyman break galaxies at  $z = 3$ . The most massive galaxies at  $z = 2$  have stellar masses  $\gtrsim 10^{11} M_\odot$ , and their observed-frame  $G - R$  colors lie in the range  $0.0 < G - R < 1.0$ . They typically have been continuously forming stars with a rate exceeding  $30 M_\odot \text{ yr}^{-1}$  over a few Gyrs from  $z = 10$  to  $z = 2$ , although the TVD simulation indicates a more sporadic star formation history than the SPH simulations. Of order half of their stellar mass was already assembled by  $z \sim 4$ . The bluest galaxies with colors  $-0.2 < G - R < 0.0$  at  $z = 2$  are somewhat less massive, with  $M_{\text{star}} < 10^{11} h^{-1} M_\odot$ , and lack a prominent old stellar population. On the other hand, the reddest massive galaxies at  $z = 2$  with  $G - R \geq 1.0$  and  $M_{\text{star}} > 10^{10} h^{-1} M_\odot$  completed the build-up of their stellar mass by  $z \sim 3$ . Interestingly, our study indicates that

---

<sup>1</sup>Harvard-Smithsonian Center for Astrophysics, 60 Garden Street, Cambridge, MA 02138, U.S.A.  
Email: knagamin@cfa.harvard.edu

<sup>2</sup>Princeton University Observatory, Princeton, NJ 08544, U.S.A.

<sup>3</sup>Institute of Astronomy, University of Cambridge, Madingley Road, Cambridge, CB3, OHA, UK

<sup>4</sup>Max-Planck-Institut für Astrophysik, Karl-Schwarzschild-Straße 1, 85740 Garching bei München, Germany

the majority of the most massive galaxies at  $z = 2$  should be detectable at rest-frame ultra-violet wavelengths, contrary to some recent claims made on the basis of near-infrared studies of galaxies at the same epoch, provided the median extinction is less than  $E(B - V) < 0.3$  as indicated by surveys of Lyman break galaxies at  $z = 3$ . However, our results also suggest that the fraction of stellar mass contained in galaxies that pass the color-selection criteria used by Steidel et al. (2004) could be as low as 50% of the total stellar mass in the Universe at  $z = 2$ . Our simulations imply that the missing stellar mass is contained in fainter ( $R > 25.5$ ) and intrinsically redder galaxies. The bright end of the rest-frame  $V$ -band luminosity function of  $z = 2$  galaxies can be characterized by a Schechter function with parameters  $(\Phi^*, M_V^*, \alpha) = (1.8 \times 10^{-3}, -23.4, -1.85)$ , while the TVD simulation suggests a flatter faint-end slope of  $\alpha \sim -1.2$ . A comparison with  $z = 3$  shows that the rest-frame  $V$ -band luminosity function has brightened by about 0.5 magnitude from  $z = 3$  to  $z = 2$  without a significant change in the shape. Our results do *not* imply that hierarchical galaxy formation fails to account for the massive galaxies at  $z \gtrsim 1$ .

*Subject headings:* cosmology: theory — stars: formation — galaxies: formation — galaxies: evolution — methods: numerical

## 1. Introduction

A number of recent observational studies have revealed a new population of red, massive galaxies at redshift  $z \sim 2$  (e.g. Chen et al. 2003; Daddi et al. 2004; Franx et al. 2003; Glazebrook et al. 2004), utilizing near-infrared (IR) wavelengths which are relatively less affected by dust extinction. At the same time, a number of studies focused on the assembly of stellar mass density at high redshift by comparing observational data and semi-analytic models of galaxy formation (e.g. Poli et al. 2003; Fontana et al. 2003; Dickinson et al. 2003a). These works argued that the hierarchical structure formation theory may have difficulty in accounting for sufficient early star formation. These concerns grew with the mounting evidence for high redshift galaxy formation including the discovery of Extremely Red Objects (EROs) at  $z \geq 1$  (e.g. Elston et al. 1988; McCarthy et al. 1992; Hu & Ridgway 1994; Cimatti et al. 2003; Smail et al. 2002), sub-millimeter galaxies at  $z \geq 2$  (e.g. Smail et al. 1997; Chapman et al. 2003), Lyman break galaxies (LBGs) at  $z \sim 3$  (e.g. Steidel et al. 1999), and galaxies at  $z \gtrsim 4$ , detected either by their Lyman- $\alpha$  emission (e.g. Hu et al. 1999; Rhoads & Malhotra 2001; Taniguchi et al. 2003; Kodaira et al. 2003; Ouchi et al. 2003a) or by their optical to near-IR colors (e.g. Iwata et al. 2003; Ouchi et al. 2003b; Dickinson

et al. 2003b; Chen & Marzke 2004). We now face the important question as to whether this evidence for high-redshift galaxy formation is consistent with the concordance  $\Lambda$ CDM model.

The redshift range around  $z \simeq 2$  is a particularly interesting epoch also for another reason. The redshift interval  $1.4 < z < 2.5$  has long been known as the ‘redshift desert’ (Abraham et al. 2004; Steidel et al. 2004) for galaxy surveys, because there was no large volume limited sample of galaxies available in this regime until very recently. This is because strong emission lines from H II regions of galaxies, such as [O II]  $\lambda$ 3727, [O III]  $\lambda\lambda$  4959, 5007, H $\alpha$  and H $\beta$ , redshift out of optical wavelengths above 9300 Å. These spectral features are necessary to easily identify galaxy redshifts, allowing ground-based telescopes to benefit from the low-night sky background and high atmospheric transmission in the wavelengths range 4000 – 9000 Å.

However, recently Adelberger et al. (2004) and Steidel et al. (2004) have introduced new techniques for exploring the ‘redshift desert’, making it possible to identify a large number of galaxies efficiently with the help of a color selection criteria in the color-color plane of  $U_n - G$  vs.  $G - R$ . In this technique, galaxies at  $z = 2 - 2.5$  are located photometrically from the mild drop in the  $U_n$  filter owing to the Ly- $\alpha$  forest opacity, and galaxies at  $z = 1.5 - 2$  are recognized from the lack of a break in their observed-frame optical spectra. The large sample of galaxies identified by these authors at  $z = 2$  makes it now possible to study galaxy formation and evolution for over 10 Gyrs of cosmic time, from redshift  $z = 3$  to  $z = 0$ , without a significant gap. We note that the epoch around  $z = 2$  is particularly important for understanding galaxy evolution because at around this time, the number density of quasi-stellar objects (QSOs) peaked (e.g. Schmidt 1968; Schmidt et al. 1995; Fan et al. 2001) and the ultra-violet (UV) luminosity density began its decline by about an order of magnitude from  $z \sim 2$  to  $z = 0$  (e.g. Lilly et al. 1996; Connolly et al. 1997; Sawicki et al. 1997; Treyer et al. 1998; Pascarelle et al. 1998; Cowie et al. 1999).

These recent observational studies of galaxies at  $z = 2$ , both in the UV and near-IR wavelengths, imply a range of novel tests for the hierarchical structure formation theory. In this study, we analyze the properties of massive galaxies at  $z = 2$  formed in state-of-the-art cosmological hydrodynamic simulations of the  $\Lambda$ CDM model, and we compare them with observations.

In an earlier recent study (Nagamine et al. 2004a), we argued that, based on two different types of hydrodynamic simulations (Eulerian TVD and SPH) and the theoretical model of Hernquist & Springel (2003) (hereafter H&S model), the predicted cosmic star formation rate (SFR) density peaks at  $z \geq 5$ , with a *higher* stellar mass density at  $z = 3$  than suggested by current observations (e.g. Brinchmann & Ellis 2000; Cole et al. 2001; Cohen 2002; Dickinson

et al. 2003a; Fontana et al. 2003; Rudnick et al. 2003; Glazebrook et al. 2004), in contrast to some claims to the contrary (Poli et al. 2003; Fontana et al. 2003). We also compared our results with those from the updated semi-analytic models of Somerville et al. (2001), Granato et al. (2000), and Menci et al. (2002), and found that our simulations and the H&S model predicts an earlier peak of the SFR density and a faster development of stellar mass density compared to these semi-analytic models.

It is then interesting to examine what our simulations predict for the properties of massive galaxies at  $z \sim 2$ . In this paper, we analyze for this purpose the same set of hydrodynamic simulations that was used in Nagamine et al. (2004a), with a special focus on the most massive galaxies at this epoch. In Section 2, we briefly describe the simulations that we use. In Section 3, we summarize our method for computing spectra of simulated galaxies both in the rest-frame and the observed-frame. In Section 4, we show the color-color diagrams and color-magnitude diagrams of simulated galaxies. In Section 5 we discuss the stellar masses and number density of galaxies at  $z = 2$ . We then investigate the observed-frame  $R$ -band luminosity function and the rest-frame  $V$ -band luminosity function in Section 6, followed by an analysis of the star formation histories in Section 7. Finally, we summarize and discuss the implications of our work in Section 8.

## 2. Simulations

We will discuss results from two different types of cosmological hydrodynamic simulations. Both approaches include “standard” physics such as radiative cooling/heating, star formation, and supernova (SN) feedback, although the details of the models and the parameter choices vary considerably.

One set of simulations was performed using an Eulerian approach, which employed a particle-mesh method for the gravity and the total variation diminishing (TVD) method (Ryu et al. 1993) for the hydrodynamics, both with a fixed mesh. The treatment of the radiative cooling and heating is described in Cen (1992) in detail. The structure of the code is similar to that of Cen & Ostriker (1992, 1993), but the code has significantly improved over the years with additional input physics. It has been used for a variety of studies, including the evolution of the intergalactic medium (Cen et al. 1994; Cen & Ostriker 1999a,b), damped Lyman- $\alpha$  absorbers (Cen et al. 2003), and galaxy formation (e.g. Cen & Ostriker 2000; Nagamine, Fukugita, Cen, & Ostriker 2001a,b; Nagamine 2002).

Our other simulations were done using the Lagrangian smoothed particle hydrodynamics (SPH) technique. We use an updated version of the code GADGET (Springel et al. 2001b),

which uses an ‘entropy conserving’ formulation (Springel & Hernquist 2002) of SPH to mitigate problems with energy/entropy conservation (e.g. Hernquist 1993) and overcooling. The code also employed a subresolution multiphase model of the interstellar medium to describe self-regulated star formation which includes a phenomenological model for feedback by galactic winds (Springel & Hernquist 2003a), and the impact of a uniform ionizing radiation field (Katz et al. 1996; Davé et al. 1999). This approach has been used to study the evolution of the cosmic SFR (Springel & Hernquist 2003b), damped Lyman- $\alpha$  absorbers (Nagamine, Springel, & Hernquist 2004a,b), Lyman-break galaxies (Nagamine, Springel, Hernquist, & Machacek 2004b), disk formation (Robertson et al. 2004), emission from the intergalactic medium (Furlanetto et al. 2003, 2004a,b,c,d; Zaldarriaga et al. 2004), and the detectability of high redshift galaxies (Barton et al. 2004; Furlanetto et al. 2004e).

In both codes, at each time-step, some fraction of gas is converted into star particles in the regions that satisfy a set of star formation criteria (e.g. significantly overdense, Jeans unstable, fast cooling, converging gas flow). Upon their creation, the star particles are tagged with physical parameters such as mass, formation time, and metallicity. After forming, they interact with dark matter and gas only gravitationally as collisionless particles.

More specifically, in the TVD simulation, the star formation rate is formulated as

$$\frac{d\rho_*}{dt} = c_* \frac{\rho_{\text{gas}}}{t_*}, \quad (1)$$

where  $c_*$  is the star formation efficiency and  $t_*$  is the star formation time-scale. In the TVD N864L22 run,  $c_* = 0.075$  and  $t_* = \max(t_{\text{dyn}}, 10^7 \text{ yr})$  were used, where  $t_{\text{dyn}} = \sqrt{3\pi/(32G\rho_{\text{tot}})}$  is the local dynamical time-scale owing to gravity. At each time-step, a part of the gas in a cell is converted to a star particle according to Equation (1), provided the gas is (a) moderately overdense ( $\delta_{\text{tot}} > 5.5$ ), (b) Jeans unstable ( $m_{\text{gas}} > m_J$ ), (c) cooling fast ( $t_{\text{cool}} < t_{\text{dyn}}$ ), and (d) the flow is converging into the cell ( $\nabla \cdot \mathbf{v} < 0$ ).

On the other hand, the SPH simulations analyzed in this study parameterized the star formation rate as

$$\frac{d\rho_*}{dt} = (1 - \beta) \frac{\rho_c}{t_*}, \quad (2)$$

where  $\beta$  is the mass fraction of short-lived stars that instantly die as supernovae (taken to be  $\beta = 0.1$ ). The star formation time-scale  $t_*$  is again taken to be proportional to the local dynamical time of the gas:  $t_*(\rho) = t_0^*(\rho_{\text{th}}/\rho)^{1/2}$ , where the value of  $t_0^* = 2.1 \text{ Gyr}$  is chosen to match the Kennicutt (1998) law. In the model of Springel & Hernquist (2003a), this parameter simultaneously determines a threshold density  $\rho_{\text{th}}$ , above which a multiphase structure of the gas, and hence star formation, is allowed to develop. This physical density is  $8.6 \times 10^6 h^2 M_\odot \text{ kpc}^{-3}$  for the simulations in this study, corresponding to a comoving baryonic

overdensity of  $7.7 \times 10^5$  at  $z = 0$ . (See Springel & Hernquist 2003a, for a description of how  $\rho_{\text{th}}$  is determined self-consistently within the model.) Note that the density  $\rho_c$  that determines the star formation rate in equation (2) is actually the average density of cold clouds determined by a simplified equilibrium model of a multiphase interstellar medium, rather than the total gas density. However, in star-forming regions, the density is so high that the mean density in cold gas always dominates, being close to the total gas density.

We will further discuss the differences between our star formation recipes in the two codes in some more detail in Section 8. The cosmological parameters adopted in the simulations are intended to be consistent with recent observational determinations (e.g. Spergel et al. 2003), as summarized in Table 1 where we list the most important numerical parameters of our primary runs. While there are many similarities in the physical treatment between the two approaches (mesh TVD and SPH), we see that the TVD simulation has somewhat higher mass resolution, and the SPH somewhat higher spatial resolution. In that sense, the two approaches are complementary and results found in common are expected to be robust.

### 3. Analysis Method

We begin our analysis by identifying galaxies in the simulations as groups of star particles. Since the two simulations use inherently different methods for solving hydrodynamics, we employ slightly different methods for locating galaxies in the two types of simulations, each developed to suit the particular simulation method well. Because the stellar groups of individual galaxies are typically isolated, there is little ambiguity in their identification, such that systematic differences owing to group finding methods are largely negligible.

For the TVD simulation, we use a version of the algorithm HOP (Eisenstein & Hut 1998) to identify groups of star particles. This grouping method consists of two discrete steps: in the first step, the code computes the overdensity at the location of each particle, and in a second step, it then merges identified density peaks based on a set of overdensity threshold parameters specified by the user. There are three threshold parameters: a peak overdensity  $\delta_{\text{peak}}$  above which the density peak is identified as a candidate galaxy, an outer overdensity  $\delta_{\text{out}}$  which defines the outer contour of groups, and finally a saddle point overdensity  $\delta_{\text{sad}}$  which determines whether two density peaks within the outer density contour should be merged. Eisenstein & Hut (1998) suggest using  $(\delta_{\text{out}}, \delta_{\text{sad}}, \delta_{\text{peak}}) = (80, 200, 240)$  for identifying dark matter halos in N-body simulations.

We applied the algorithm to the star particles in our simulation using various combinations of these parameters, and found that the results do not depend very much on the

detailed choice. This reflects the higher concentration and isolation of star particle groups as compared to the dark matter, making group finding typically straightforward. However, the stellar peak overdensities relative to the mean are so high that the saddle-overdensity parameter in HOP is unimportant, and the small galaxies associated with a large central galaxy at the center of a large dark matter halo are often not well separated by this algorithm. Therefore, we decided not to apply the second step of the algorithm. Instead, we merge two density peaks identified by the first step only if they are within two neighboring cells. By visually inspecting the particle distribution of very massive dark matter halos, we found that this method succeeds in separating some of the small galaxies embedded in a large dark matter halo especially at the outskirts of the halo, and helps to somewhat mitigate the ‘overmerging problem’ in high density regions. However, even with this revised method, the central massive galaxy remains afterwards, and the addition of a small number of galaxies to the faint-end of the luminosity function does not change the qualitative feature of our results. Clearly more work is needed to improve this situation on the grouping in the future, for example, using an improved grouping method such as VOBOZ (Neyrinck, Gnedin, & Hamilton 2004).

For the SPH simulations, we employ the same method as in Nagamine et al. (2004b), where we identified isolated groups of star particles using a simplified variant of the SUBFIND algorithm proposed by Springel et al. (2001a). In short, we first compute an adaptively smoothed baryonic density field for all star and gas particles. This allows us to robustly identify centers of individual galaxies as isolated density peaks. We then find the full extent of these galaxies by processing the gas and star particles in order of declining density, adding particles one by one to the galaxies. If all of the 32 nearest neighbors of a particle have lower density, this particle is considered to be a new galaxy ‘seed’. Otherwise, the particle is attached to the galaxy that its nearest denser neighbor already belongs to. If the two nearest denser neighbors belong to different galaxies, and one of these galaxies has less than 32 particles, these galaxies are merged. If the two nearest denser neighbors belong to different galaxies and both of these galaxies have more than 32 particles, then the particle is attached to the larger group of the two, leaving the other one intact. Finally, we restrict the set of gas particles processed in this way to those particles which have at least a density of 0.01 times the threshold density for star formation, i.e.  $\rho_{\text{th}} = 8.6 \times 10^6 h^2 M_{\odot} \text{ kpc}^{-3}$  (see Springel & Hernquist 2003a, for details on how the star formation threshold is determined). Note that we are here not interested in the gaseous components of galaxies – we only include gas particles because they make the method more robust owing to the improved sampling of the baryonic density field.

We found that the above method robustly links star particles that belong to the same isolated galaxy in SPH simulations. A simpler friends-of-friends algorithm with a small

linking length can achieve a similar result, but the particular choice one needs to make for the linking length in this method represents a problematic compromise, either leading to artificial merging of galaxies if it is too large, or to loss of star particles that went astray from the dense galactic core, if it is too small. Note that, unlike in the detection of dark matter substructures, no gravitational unbinding algorithm is needed to define the groups of stars that make up the galaxies formed in the simulations. We consider only galaxies with at least 32 particles (star and gas particles combined) in our subsequent analysis.

For both simulations, each star particle is tagged with its mass, formation time, and metallicity of the gas particle that it was spawned from. Based on these three tags, we compute the emission from each star particle, and co-add the flux from all particles for a given galaxy to obtain the spectrum of the simulated galaxy. We use the population synthesis model by Bruzual & Charlot (2003) which assumes a Chabrier (2003b) initial mass function (IMF) within a mass range of  $[0.1, 100] M_{\odot}$ , as recommended by Bruzual & Charlot (2003). Spectral properties obtained with this IMF are very similar to those obtained using the Kroupa (2001) IMF, but the Chabrier (2003b) IMF provides a better fit to counts of low-mass stars and brown dwarfs in the Galactic disk (Chabrier 2003a). We use the high resolution version of the spectral library of Bruzual & Charlot (2003) which contains 221 spectra describing the spectral evolution of a simple stellar population from  $t = 0$  to  $t = 20$  Gyr over 6900 wavelength points in the range of 91 Å- 160  $\mu\text{m}$ .

Once the intrinsic spectrum is computed, we apply the Calzetti et al. (2000) extinction law with three different values of  $E(B - V) = 0.0, 0.15, 0.3$  in order to investigate the impact of extinction. These values span the range of extinction estimated from observations of LBGs at  $z = 3$  (Adelberger & Steidel 2000; Shapley et al. 2001). Using the spectra computed in this manner, we then derive rest-frame colors and luminosity functions of the simulated galaxies.

To obtain the spectra in the observed frame, we redshift the spectra and apply absorption by the intergalactic medium (IGM) following the prescription of Madau (1995). Once the redshifted spectra in the observed frame are obtained, we convolve them with different filter functions, including  $U_n, G, R$  (Steidel & Hamilton 1993) and standard Johnson bands, and compute the magnitudes in both AB and Vega systems. Apparent  $U_n, G, R$  magnitudes are computed in the AB system to compare our results with Adelberger et al. (2004) and Steidel et al. (2004), while the rest-frame V-band magnitude is computed in the Vega system.



#### 4. Color-color & color-magnitude diagrams

In Figure 1, we show the color-color diagrams of simulated galaxies at  $z = 2$  in the observed-frame  $U_n - G$  vs.  $G - R$  plane, for both SPH (top 2 panels) and TVD (bottom right panel) simulations. Only galaxies brighter than  $R = 25.5$  are shown in order to match the magnitude limit of the sample of Steidel et al. (2004). We plot different symbols for three different values of Calzetti extinction:  $E(B - V) = 0.0$  (blue dots), 0.15 (green crosses), and 0.3 (red open squares). As the level of extinction by dust is increased from  $E(B - V) = 0.0$  to 0.3, the measured points move towards the upper right corner of each panel. This behavior is expected for a conventional star-forming galaxy spectrum, as demonstrated in Figure 2 of Steidel et al. (2003). The color-selection criteria used by Adelberger et al. (2004) and Steidel et al. (2004) is shown by the long-dashed boxes. The upper (lower) box corresponds to their BX (BM) criteria for selecting galaxies at  $z = 2.0 - 2.5$  ( $z = 1.5 - 2.0$ ). The number density of all the galaxies shown (i.e.  $R < 25.5$ ) is given in each panel for  $E(B - V) = 0.0, 0.15, 0.30$  from top to bottom, respectively.

It is encouraging to see that in all the panels most of the simulated galaxies actually satisfy the observational color selection criteria for the case of  $E(B - V) = 0.15$ . This suggests that the simulated galaxies have realistic UV colors compared to the observed ones. Simulated galaxies with no extinction tend to be too blue compared to the color-selection criteria. In the SPH G6 run, the distribution is wider than in the SPH D5 and TVD N864L22 runs, owing to the larger number of galaxies in a larger simulation box, and the distribution actually extends beyond the color selection boundaries. The spatial number density of galaxies with  $R < 25.5$  is about  $2 \times 10^{-2} h^3 \text{ Mpc}^{-3}$  for the SPH G6 run. We will discuss the number density of galaxies with various cuts in Figure 4 in more detail.

We repeated the same calculation with the Sloan Digital Sky Survey’s  $u, g, r, i, z$  filter set, and found that the distribution of points hardly changes, even when we exchange  $U_n - G$  with  $u - g$ , and  $G - R$  with  $g - r$ . This means that searches for galaxies in the redshift range  $1.4 < z < 2.5$  can also substitute the Sloan filters  $u, g, r$  when applying a color-selection following the ‘BX’ and ‘BM’ criteria adopted by Adelberger et al. (2004) and Steidel et al. (2004).

In Figure 2, we show the simulated galaxies at  $z = 2$  in the plane of apparent  $R$  magnitude and  $G - R$  color. Again, we use three different symbols for three different values of extinction:  $E(B - V) = 0.0$  (blue dots), 0.15 (green crosses), and 0.3 (red open squares). The vertical long-dashed line and the arrow indicate the magnitude limit of  $R = 25.5$  used by Steidel et al. (2004). The horizontal line at  $G - R = 0.75$  corresponds to the upper limit of the color-selection box of Steidel et al. (2004) and Adelberger et al. (2004).

We see that most of the galaxies brighter than  $R = 25.5$  automatically satisfy the criterion  $G - R < 0.75$ , and almost no galaxies with  $R < 25.5$  fall out of the region for  $E(B - V) = 0.15$ . There is a significant population of dim ( $R > 27$ ) galaxies with  $G - R > 1$ . We will see below that these are low-mass galaxies with stellar masses  $M_{\text{star}} \leq 10^{10} h^{-1} M_{\odot}$ . We will discuss the amount of stellar mass contained in the galaxies that satisfy the color selection criteria in Section 5.

## 5. Galaxy stellar masses at $z = 2$

In Figure 3, we show the apparent  $R_{AB}$  magnitude vs. stellar mass of simulated galaxies at redshift  $z = 2$ , for both SPH (top 2 panels) and TVD (bottom right panel) simulations. The three different symbols correspond to three different values of extinction:  $E(B - V) = 0.0$  (blue dots), 0.15 (green crosses), and 0.3 (red open squares). The vertical long-dashed line and the arrow indicate the magnitude limit of  $R = 25.5$  used by Steidel et al. (2004).

From this figure, we see that there are many galaxies with stellar masses larger than  $10^{10} h^{-1} M_{\odot}$  and  $R < 25.5$  at  $z = 2$  in our simulations. In the SPH G6 run, the masses of the most luminous galaxies are substantially larger than those in the D5 run. But this is primarily a result of a finite box size effect; the brightest galaxies have a very low space-density, and so they are simply not found in simulations with too small a volume. In the SPH G6 run, the most massive galaxies at  $z = 2$  have masses  $10^{11} < M_{\text{star}} < 10^{12} h^{-1} M_{\odot}$  with a number density of  $3.5 \times 10^{-4} h^3 \text{ Mpc}^{-3}$ . Such galaxies are hence not commonly found in a comoving box-size of  $\sim (30 \text{ Mpc})^3$ , in fact, only one such galaxy exists in the D5 run. Cosmic variance hence significantly affects the resulting number density, and one ideally needs a simulation box larger than  $\simeq (100 h^{-1} \text{ Mpc})^3$  to obtain a reliable estimate of the number density of such massive galaxies. We note however that a couple of such massive galaxies are also found in the TVD N864L22 run, which is presumably in part a result of overmerging owing to the relatively large cell size compared to the gravitational softening length of the D5 run.

In Figure 4, we summarize the results on the cumulative number densities of galaxies, either measured above a certain threshold value of stellar mass [panel (a)], or below a threshold value of observed-frame  $R$ -band magnitude [panel (b)], or rest-frame  $V$ -band magnitude [panel (c)]. In panel (a), we see that the results of different runs agree reasonably well in the threshold mass range of  $10^9 < M_{\text{star}} < 10^{10} h^{-1} M_{\odot}$ , but differ somewhat at the lower and higher mass thresholds. At the low-mass end, the lower resolution of the G6 run results in a lower number density than in the D5 run. At the high-mass end, the smaller box-size limits the number density in the D5 run compared to the higher value in the G6 run. The result of

the TVD run falls in between those of D5 and G6 at the low-mass end, but gives larger values relative to the SPH runs at the high-mass end, probably owing to the overmerging problem. A similar level of agreement can be seen in panel (c), where the rest-frame magnitude is used for the  $x$ -axis, but in panel (b), comparatively large differences are present partly owing to the larger stretch in the abscissa.

We find that the amount of stellar mass contained in the galaxies that satisfy the color-selection criteria is in general far from being close to the total stellar mass. Owing to the limited box-size and resolution effects, it is somewhat difficult to obtain an accurate estimate of the mass fraction above some magnitude limit. However, we list the stellar mass fractions as a reference for future work. In the G6 run, which has comparatively low mass resolution, the stellar mass fraction contained in galaxies that pass the criteria (i.e.  $R < 25.5$  & color-selection) account for only (60, 65, 42)% of all the stars, for extinctions of  $E(B - V) = (0.0, 0.15, 0.3)$ , respectively. These fractions are relatively large compared to other runs, because, as we will see in Section 6, the luminosity function in the G6 run starts to fall short of galaxies near  $R \sim 25.5$  compared to the D5 run owing to its limited resolution, and the G6 run lacks low-mass faint galaxies with  $R > 25.5$ . On the other hand, in the D5 run, the stellar mass fraction contained in galaxies that pass the criteria (i.e.  $R < 25.5$  & color-selection) account for only (32, 17, 2)% and (16, 13, 1)% of the stars in the TVD N864L22 run, for extinctions of  $E(B - V) = (0.0, 0.15, 0.3)$ , respectively. These fractions are smaller compared to those of the G6 run, because the D5 and TVD N864L22 runs lack massive bright galaxies owing to their smaller box sizes. If we relax the criteria from ‘ $R < 25.5$  & color-selection’ to ‘only  $R < 25.5$ ’, then the corresponding stellar mass fractions increase to (75, 65, 44)% for G6, (32, 17, 3)% for D5, and (46, 34, 29)% for TVD N864L22. In summary, we expect that the true stellar mass fraction that satisfies the criteria lies somewhere between the results of G6 and D5 (and TVD N864L22) runs, which should be roughly  $\sim 50\%$ .

This implies that the current surveys with a magnitude limit of  $R \sim 25.5$  at best account for half of the stellar mass in the Universe. Nagamine et al. (2004a) reached a similar conclusion based on different theoretical arguments that compared the results of our hydrodynamic simulations and the theoretical model of Hernquist & Springel (2003) with near-IR observations of galaxies (e.g. Cole et al. 2001; Dickinson et al. 2003a; Fontana et al. 2003; Rudnick et al. 2003; Glazebrook et al. 2004). Franx et al. (2003) and Daddi et al. (2004) suggested that the unaccounted-for contribution to the stellar mass might be hidden in a red population of galaxies. Our simulation suggests that the missed stellar masses are mostly contained in the fainter ( $R > 25.5$ ) and redder galaxies. But note that we have not considered large values of extinction with  $E(B - V) > 0.3$ .

In Figure 5, we show the observed-frame  $G - R$  color vs. stellar mass of simulated galaxies at  $z = 2$  for both SPH (top 2 panels) and TVD (bottom right panel) simulations. Here, only the case of  $E(B - V) = 0.15$  is shown. In the top two panels for the SPH runs, the red open crosses show the galaxies that are brighter than  $R = 25.5$ , and the blue dots show the rest of the galaxies. The discrete stripes seen at low-mass end of the distribution for the SPH runs are due to the discreteness of the star particles in the simulation. For the TVD run, there is a strong concentration of points at  $G - R \sim 1.4$ , which we will discuss in detail in Section 7.

An interesting point to note in this figure is that the bluest galaxies at  $z = 2$  are not necessarily the most massive ones. Rather, the bluest galaxies with colors  $-0.2 < G - R < 0.2$  are galaxies with somewhat lower mass in the range  $M_{\text{star}} < 10^{10} h^{-1} M_{\odot}$ . The most massive galaxies with  $M_{\text{star}} \gtrsim 10^{10} h^{-1} M_{\odot}$  have slightly redder colors of  $0.2 < G - R < 0.6$  owing to their underlying old stellar population.

In the TVD simulation, there are a couple of galaxies with  $G - R > 2.0$  and  $M_{\text{star}} > 10^{10} h^{-1} M_{\odot}$ , which are absent in the SPH simulations. These galaxies are dominated by the old stellar population because they have completed their star formation before  $z \sim 3$  as we will see in Section 7.

## 6. Galaxy luminosity functions

Figure 6 shows the observed-frame  $R$ -band luminosity function for all simulated galaxies at  $z = 2$  in both SPH (top 2 panels) and the TVD (bottom left panel) simulations. In these 3 panels, blue long-dashed, green solid, and red dot-short-dashed lines correspond to  $E(B - V) = 0.0, 0.15, 0.30$ , respectively. The vertical dotted lines indicate the magnitude limit of  $R = 25.5$  used by Steidel et al. (2004). In the bottom right panel, a combined result is shown with the SPH D5 (green solid line), G6 (red long-dashed line), and TVD (blue dot-dashed line) results overplotted for the case of  $E(B - V) = 0.15$ . For comparison, Schechter functions with the following parameters (simply chosen by eyeball fit) are shown as short-dashed lines:  $(\Phi^*, M_R^*, \alpha) = (1 \times 10^{-2}, 23.2, -1.4)$  for SPH D5 & G6 runs (top two panels) and the combined results (bottom right panel), and  $(1 \times 10^{-2}, 24.5, -1.4)$  for TVD (bottom left), respectively.

The bottom right panel of Figure 6 gives a relative comparison between the different runs. We see that the SPH G6 run contains a larger number of luminous galaxies with  $R < 25$  compared to the other runs, an effect that results from its larger box-size. On the other hand, the G6 run lacks fainter galaxies at  $R > 25$  compared to D5 run owing to

its limited mass resolution. The SPH G6 run hence covers the bright-end of the Schechter function with  $M_R^* = 23.2$ , while the D5 run covers better the faint-end of the luminosity function with a slope of  $\alpha = -1.4$ . The TVD N864L22 run agrees with the D5 results at the bright-end near  $R = 25$ , but the deviation from the D5 result starts to become somewhat large at  $R > 28$ . We will discuss a number of possible reasons for these differences between the SPH and TVD runs in Section 8.

In Figure 7, we show the rest-frame  $V$ -band luminosity function of all simulated galaxies at  $z = 2$  for both SPH (top 2 panels) and TVD (bottom left panel) simulations. In these three panels, blue long-dashed, green solid, and red dot-short-dashed lines correspond to extinctions of  $E(B - V) = 0.0, 0.15, 0.30$ , respectively. In the bottom right panel, the combined result is shown with the SPH D5 (green solid line), G6 (red long-dashed), and TVD (blue dot-dashed) runs overplotted for the case of  $E(B - V) = 0.15$ . For reference, the magnitude limit of  $M_V = -21.2$  (for  $h = 0.7$ ) for the survey of  $z = 3$  LBGs by Shapley et al. (2001) is indicated by the vertical dotted line and the arrow. For comparison, we also include Schechter function fits with parameters  $(\Phi^*, M_V^*, \alpha) = (1.8 \times 10^{-3}, -23.4, -1.8)$  as short-dashed curves in all panels. These Schechter parameters are the same as the ones that Shapley et al. (2001) fitted to their observational data, except that the characteristic magnitude  $M_V^*$  is 0.5 magnitudes brighter. The same amount of brightening is seen in the G6 run from  $z = 3$  (see Fig. 5 of Nagamine et al. (2004b)<sup>1</sup>) to  $z = 2$ . So the G6 run with  $E(B - V) = 0.15$  describes the bright-end of the luminosity function at  $z = 2$  and  $z = 3$  quite well. In the bottom left panel for the TVD run, another Schechter function with a much shallower faint-end slope and parameters  $(\Phi^*, M_V^*, \alpha) = (3.5 \times 10^{-2}, -22.5, -1.15)$  is also shown with a magenta long-dash-short-dashed line for comparison. One can see that the TVD run contains more fainter galaxies with  $M_V > -15$  than the SPH runs. This could be due to the higher baryonic mass resolution and the additional small-scale power in the TVD run compared with the SPH runs as we will discuss more in Section 7.

We can compute the expected characteristic magnitude  $M_R^*$  of  $z = 2$  galaxies from the observational estimate of  $M_R^*$  at  $z = 3$ . The difference in the luminosity distance between  $z = 3$  and  $z = 2$  corresponds to about one magnitude for our adopted cosmology, and we saw in the previous paragraph that the rest-frame  $V$ -band luminosity function brightened by  $\sim 0.5$  magnitude from  $z = 3$  to  $z = 2$ . Therefore, we expect that  $M_R^*$  should be brighter by about 1.5 magnitudes at  $z = 2$  compared to  $z = 3$ . Adelberger & Steidel (2000) reported

---

<sup>1</sup>We note that there was an error in the calculation of the AB magnitudes in Nagamine et al. (2004b). An additional factor of  $5 \log(1+z) = 3.01$  has to be added to obtain correct AB magnitudes. The corrected version of the paper will be posted at astro-ph/0311295. The rest-frame  $V$ -band results were not affected by this error.

$M_R^* = 24.54$  for the observed-frame  $R$ -band luminosity function of the  $z = 3$  galaxies. Therefore we obtain  $M_R^* \sim 23.0$  as the expected value for the  $z = 2$  galaxies. The result of the SPH G6 run shown in Fig. 6 is reasonably close to this expected value. It is also clear that the box size of the D5 and TVD runs are too small to reliably sample the brightest galaxies at  $z = 2$ . This is also seen in Fig. 7 as a lack of brightest galaxies at  $M_V < -23$  in the D5 and TVD runs. This is because the brightest galaxies form in rare high density peaks which are at the knots of the large-scale filaments, and one needs a sufficiently large volume to sample a fair number of such bright galaxies reliably. Since the comoving correlation length of LBGs at  $z = 3$  are  $\sim 4h^{-1}$  Mpc (Adelberger et al. 2003), one needs a box size larger than at least  $L_{\text{box}} \gtrsim 40h^{-1}$  Mpc in order to have a fair sample of LBGs at  $z = 3$ . The simulated volume of the G6 run is  $(100h^{-1} \text{ Mpc})^3$  comoving, and one of the face of the simulation box corresponds to  $2.5 \text{ deg}^2$  at  $z = 3$ . The coverage area of the LBG survey of Steidel et al. (2003) at  $z = 3$  is about  $0.4 \text{ deg}^2$ , and the depth of their survey is  $\Delta z \simeq 0.5$  which corresponds to  $\sim 500h^{-1}$  Mpc comoving for our adopted flat- $\Lambda$  cosmology. Therefore the volumes of the G6 simulation and the Steidel et al. survey are comparable.

## 7. Star formation history of galaxies

In Figures 8, 9, and 10, we show the star formation (SF) histories of massive galaxies at  $z = 2$  as a function of cosmic age, for the SPH D5, G6, and TVD runs, respectively. In these figures, panels (a) & (b) show results for the two most massive galaxies in each simulation box, while panels (c) & (d) are for the two reddest galaxies among those with  $M_{\text{star}} > 10^{10}h^{-1}M_{\odot}$ . In the right side of each panel, the following quantities for the case of  $E(B - V) = 0.15$  are listed from top to bottom: stellar mass in units of  $h^{-1}M_{\odot}$ , rest-frame V-band magnitude, observed-frame  $R$ -band magnitude, and  $G - R$  color. In panel (e), the cumulative star formation history of the galaxies in panels (a) – (d) is shown.

The results of the SPH D5 and G6 runs (Fig. 8 & 9) suggest that the most massive galaxies have almost continuously formed stars with a rate exceeding  $30 M_{\odot} \text{ yr}^{-1}$  over a few Gyrs from  $z = 10$  to  $z = 2$  (note that  $30 M_{\odot} \text{ yr}^{-1} \times 3 \text{ Gyr} \sim 10^{11}M_{\odot}$ ). Half of their stellar mass was already assembled by  $z = 4$ . The reddest galaxies (panels (c) & (d)) have colors of  $G - R \gtrsim 1.0$ , and their star formation has become less active after  $z = 3$ , with the bulk of their stellar mass created before  $z = 3$  as can be seen in the panel (e).

The TVD simulation (Fig. 10) on the other hand suggests a more sporadic star formation history than the SPH simulations, and the two most massive galaxies in the simulation box experienced massive star formation between  $z = 3$  and  $z = 2$  that exceeded  $1000 M_{\odot} \text{ yr}^{-1}$  for brief periods. The peak star formation rate of the most massive galaxy in the G6 run

also reaches  $1000 M_{\odot} \text{ yr}^{-1}$  occasionally. In the real universe, such violent starburst activity is found in high-redshift quasars and submm sources where the existence of dense, warm, and massive molecular clouds of  $10^{10} - 10^{11} M_{\odot}$  is inferred from the observed rotational emission line of CO (e.g. Omont et al. 2003; Beelen et al. 2004). The number density of quasar host galaxies with such a violent star formation activity is not well-constrained yet, but it probably is not very large because the space density of quasars with  $M_B < -26$  is smaller than  $n_Q \sim 10^{-6} \text{ Mpc}^{-3}$  (e.g. Pei 1995). The space density of submm sources is also similar:  $n_{\text{submm}} \sim 6.5 \times 10^{-6} \text{ Mpc}^{-3}$  at  $z \sim 2$  (Chapman et al. 2003). These values are much smaller than the space density of Lyman break galaxies  $n_{\text{LBG}} \sim 4 \times 10^{-3} h^3 \text{ Mpc}^{-3}$  (Adelberger et al. 2004). Finding 3 such massive starbursts at  $z = 2$  in our TVD simulation box of  $(22h^{-1} \text{ Mpc})^3$  results in a number density of  $\sim 3 \times 10^{-4} h^3 \text{ Mpc}^{-4}$ , which may be too high compared to the observed value. It is also possible that the two galaxies shown in Figure 10 are affected by the overmerging problem which tends to merge galaxies in very high density regions owing to a lack of spatial resolution. If these two massive galaxies were broken up into several less massive galaxies, then the  $1000 M_{\odot} \text{ yr}^{-1}$  of star formation would be distributed to a few hundreds  $M_{\odot} \text{ yr}^{-1}$  for each galaxy.

The two reddest massive galaxies in the TVD run (Fig. 10c & 10d) have cumulative star formation histories which are similar to those of the SPH runs, with half of their stellar mass already assembled by  $z \sim 4$ . They have completed their star formation by  $z \sim 3$  and have been quiet from  $z = 3$  to  $z = 2$ . Because they are dominated by an old stellar population, they have very red colors of  $G - R > 2.0$  and show up in the upper right corner of the TVD (bottom right) panel in Fig. 1.

Another way of looking at the star formation history of galaxies is to look at the distribution of formation times of stellar particles in the simulation for a given set of galaxies as a whole; i.e. we here analyze the combined star formation history for a particular class of galaxies divided by their stellar mass. In Figure 11, we show the mass-weighted probability distribution of stellar masses as a function of formation time ( $t_{\text{form}} = 0$  corresponds to the Big Bang), for different samples of galaxies. To this end, we have split the total galaxy sample into 3 categories by stellar mass at  $z = 2$ :  $M_{\text{star}} > 10^{10} h^{-1} M_{\odot}$  (top panel),  $10^9 < M_{\text{star}} < 10^{10} h^{-1} M_{\odot}$  (middle panel), and  $M_{\text{star}} < 10^9 h^{-1} M_{\odot}$  (bottom panel). Different line types correspond to different simulations: red long-dashed (SPH G6 run), blue solid (SPH D5 run), and black dot-dashed (TVD N864L22 run). The vertical dotted lines indicate four different epochs, namely  $z = 2, 3, 4, \& 5$ , as indicated in the top panel.

In the two top panels for massive galaxies, the distribution roughly agrees between the different runs, except for the large bump in the TVD run close to  $z = 2$ , which is caused by starbursts in a few massive galaxies. Also note that the distribution of G6 run is slightly

more bumpy owing to lack of mass resolution compared to other runs.

In the bottom panel for the less massive galaxies, the distribution is very different between the 3 runs. In the TVD run, the bulk of stars in low-mass galaxies forms before  $z = 4$ , whereas the opposite is true for the SPH G6 run. These low-mass galaxies that formed very early on appeared as a strong concentration of points at  $G - R \sim 1.2$  in Fig. 5 for the TVD N864L22 run. The result for the SPH D5 appears to be intermediate between the two. This could perhaps be caused by the additional small-scale power in the TVD run compared with the SPH runs. The initial mean inter-particle separations of both dark matter and gas particles in the two SPH runs are comoving 104 and 206  $h^{-1}$  kpc for the D5 and G6 run, respectively, but the mean inter-particle separation of dark matter particles in the TVD run is comoving 51  $h^{-1}$  kpc, with a baryonic cell size of 25  $h^{-1}$  kpc. Therefore, at very early times, the TVD run should be able to resolve smaller matter fluctuations than the two SPH runs. Such an effect could explain the earlier formation epoch of low-mass galaxies in the TVD run compared to the two SPH runs, provided it is not compensated by the comparatively lower gravitational force resolution (roughly 2 cells) of the TVD particle-mesh method.

## 8. Discussion & Conclusions

We have used two different types of hydrodynamic cosmological simulations (Eulerian TVD and SPH) to study the properties of massive galaxies at  $z = 2$  in a  $\Lambda$ CDM universe, with particular emphasis on an observationally inspired selection based on the  $U_n, G, R$  filter set. The simulated galaxies at  $z = 2$  satisfy well the color-selection criteria proposed by Adelberger et al. (2004) and Steidel et al. (2004) when we assume Calzetti et al. (2000) extinction with  $E(B - V) = 0.15$ . However, we find that the fraction of stellar mass contained in galaxies that pass the color-selection criteria could be as low as 50% of the total. The number density of simulated galaxies brighter than  $R < 25.5$  at  $z = 2$  is about  $2 \times 10^{-2} h^3 \text{ Mpc}^{-3}$  for  $E(B - V) = 0.15$  in the most representative run (SPH G6 run), roughly one order of magnitude larger than that of Lyman break galaxies at  $z = 3$ . The increase of the number density of bright galaxies can be viewed as a consequence of the ongoing hierarchical build-up of larger and brighter galaxies with ever more stellar mass.

The most massive galaxies at  $z = 2$  have stellar masses of  $\gtrsim 10^{11} M_\odot$ , and their observed-frame  $G - R$  colors lie in the range  $0.0 < G - R < 1.0$  provided that the median extinction is  $E(B - V) \sim 0.15$ . They have been continuously forming stars with a rate exceeding  $30 M_\odot \text{ yr}^{-1}$  over a few Gyrs from  $z = 10$  to  $z = 2$ . Typically, half of their stellar mass was already assembled by  $z \sim 4$ . The bluest galaxies with  $-0.2 < G - R < 0.0$  at  $z = 2$  are somewhat less massive, with  $M_{\text{star}} < 10^{11} h^{-1} M_\odot$ , and are less dominated by old stellar



populations. Our study suggests that the majority of the most massive galaxies at  $z = 2$  could be detected at rest-frame UV wavelengths contrary to some recent claims based on near-IR studies (e.g. Franx et al. 2003; van Dokkum et al. 2004) of galaxies at the same epoch, provided the median extinction is in the range  $E(B - V) < 0.3$  as indicated by the surveys of Lyman break galaxies at  $z = 3$ . We plan to extend our analysis to the near-IR pass-bands in subsequent work. We find that these massive galaxies reside in the highest overdensity regions in the simulations at  $z = 2$ .

While it is encouraging to see that the two very different types of hydrodynamic simulation methods give a similar picture for the overall properties of massive galaxies at  $z = 2$ , we have also seen some notable differences in the results of the SPH and TVD simulations throughout the paper.

For example, the star formation history of galaxies in the TVD simulation is clearly more sporadic or ‘bursty’ than that in the SPH simulations. This probably owes to the differences in resolution and the details of how star formation is modeled in the two codes, as we described in Section 2. While the dependence of the star formation rate on local gas density is essentially the same for the TVD and SPH simulations, the different numerical coefficients effectively multiplying the local density on the right hand sides of Equations (1) and (2) produce different temporal smoothing of the local star formation rates and the parameters adopted by the TVD code leads to a more ‘bursty’ output ( $\dot{\rho}_*^{\text{TVD}}/\dot{\rho}_*^{\text{SPH}} \simeq 3.8$ ), although not to a significantly different total star formation rate. At this point we simply must await a more detailed theory or be guided by observations in choosing between the two approaches.

Another difference we saw is that the faint-end slope of the rest-frame  $V$ -band luminosity function: the TVD simulation gives  $\alpha = -1.15$ , similar to what is observed locally  $\alpha = -1.2$  (e.g. Blanton et al. 2001), but the SPH D5 and G6 runs give much steeper slope of  $\alpha = -1.8$ . The question of the nature of the faint-end slope of the luminosity function is one that we have not resolved at this point. The difference may owe to the difference in the treatment of feedback, but Chiu et al. (2001) found a flat faint-end slope of  $\alpha = -1.2$  in a high-resolution softened Lagrangian hydrodynamic (SLH) simulation (Gnedin 1995) even when the code did not include SN feedback, suggesting that the photoionization of the gas in low-mass halos by the UV background radiation field is responsible for suppressing the formation of low-mass galaxies (see also Thoul & Weinberg 1996; Quinn et al. 1996; Bullock et al. 2000). Thus the theoretical expectation is not fully clear at present, and it will be very interesting to see what is indicated by upcoming observational programs of deeper high redshift galaxies and future theoretical studies.

The present study shows that despite a considerably different numerical methodology

and large differences in the assumed model for star formation, two independent hydrodynamic codes predict the formation of rather massive galaxies at  $z \simeq 2$  in the  $\Lambda$ CDM cosmology, with properties that are broadly consistent with current observations. The results do not suggest that hierarchical galaxy formation fails to be able to account for these objects. On the contrary, it predicts that significant additional mass in galaxies will be found as the observational selection criteria are broadened.

We thank Scott Burles, Hsiao-Wen Chen, Masataka Fukugita, Max Pettini, Alice Shapley, and Rob Simcoe for enlightening discussions. We also thank Nick Gnedin for refereeing the paper and for constructive comments on the manuscript. This work was supported in part by NSF grants ACI 96-19019, AST 00-71019, AST 02-06299, and AST 03-07690, and NASA ATP grants NAG5-12140, NAG5-13292, and NAG5-13381. The SPH simulations were performed at the Center for Parallel Astrophysical Computing at Harvard-Smithsonian Center for Astrophysics. The TVD simulations were performed at the National Center for Supercomputing Applications (NCSA).

## REFERENCES

- Abraham, R. G., Glazebrook, K., and D. Crampton, P. J. M., Murowinski, R., Jørgensen, I., Roth, K., Hook, I. M., Savaglio, S., Chen, H.-W., et al. 2004, *AJ*, 127, 2455
- Adelberger, K. L. & Steidel, C. C. 2000, *ApJ*, 544, 218
- Adelberger, K. L., Steidel, C. C., Shapley, A. E., Hunt, M. P., Erb, D. K., Reddy, N. A., & Pettini, M. 2004, *ApJ*, in press (astro-ph/0401445)
- Adelberger, K. L., Steidel, C. C., Shapley, A. E., & Pettini, M. 2003, *ApJ*, 584, 45
- Barton, E. J., Davé, R., Smith, J.-D. T., Papovich, C., Hernquist, L., & Springel, V. 2004, *ApJ*, 605, L1
- Beelen, A., Cox, P., Pety, J., Carilli, C. L., Bertoldi, F., Momjian, E., Omont, A., Petitjean, P., & Petric, A. O. 2004, *A&A*, submitted (astro-ph/0404172)
- Blanton, M. R., Dalcanton, J., Eisenstein, D., Loveday, J., Strauss, M. A., SubbaRao, M., Weinberg, D. H., Anderson, J. E. J., Annis, J., Bahcall, N., et al. 2001, *AJ*, 121, 2358
- Brinchmann, J. & Ellis, R. 2000, *ApJ*, 536, L77
- Bruzual, G. & Charlot, S. 2003, *MNRAS*, 344, 1000

- Bullock, J. S., Kravtsov, A. V., & Weinberg, D. H. 2000, *ApJ*, 539, 517
- Calzetti, D., Armus, L., Bohlin, R. C., Kinney, A. L., Koornneef, J., & Storchi-Bergmann, T. 2000, *ApJ*, 533, 682
- Cen, R. 1992, *ApJS*, 78, 341
- Cen, R., Miralda-Escude, J., Ostriker, J. P., & Rauch, M. 1994, *ApJ*, 437, L9
- Cen, R. & Ostriker, J. P. 1992, *ApJ*, 399, L113
- . 1993, *ApJ*, 417, 404
- . 1999a, *ApJ*, 514, 1
- . 1999b, *ApJ*, 519, L109
- . 2000, *ApJ*, 538, 83
- Cen, R., Ostriker, J. P., Prochaska, J. X., & Wolfe, A. M. 2003, *ApJ*, 598, 741
- Chabrier, G. 2003a, *ApJ*, 586, L133
- . 2003b, *PASP*, 115, 763
- Chapman, S. C., Blain, A. W., Ivison, R. J., & Smail, I. R. 2003, *Nature*, 422, 695
- Chen, H.-W. & Marzke, R. 2004, *ApJL*, submitted (astro-ph/0405432)
- Chen, H.-W., Marzke, R., McCarthy, P. J., Martini, P., Carlberg, R. G., Persson, S. E., Bunker, A., Bridge, C. R., & Abraham, R. G. 2003, *ApJ*, 586, 745
- Chiu, W. A., Gnedin, N. Y., & Ostriker, J. P. 2001, *ApJ*, 563, 21
- Cimatti, A., Daddi, E., Cassata, P., Pignatelli, E., Fasano, G., Vernet, J., Fomalont, E., Kellermann, K., Zamorani, G., Mignoli, M., et al. 2003, *A&A*, 412, L1
- Cohen, J. G. 2002, *ApJ*, 567, 672
- Cole, S., Norberg, P., Baugh, C. M., Frenk, C. S., Bland-Hawthorn, J., Bridges, T., Cannon, R., Colless, M., Collins, C., Couch, W., et al. 2001, *MNRAS*, 326, 255
- Connolly, A. J., Szalay, A. S., Dickinson, M. E., SubbaRao, M. U., & Brunner, R. J. 1997, *ApJ*, 486, L11
- Cowie, L. L., Songaila, A., & Barger, A. J. 1999, *AJ*, 118, 603

- Daddi, E., Cimatti, A., Renzini, A., Vernet, J., Conselice, C., Pozzetti, L., Mignoli, M., Tozzi, P., Broadhurst, T., de Serego Alighieri, S., et al. 2004, *ApJ*, 600, L127
- Davé, R., Hernquist, L., Katz, N., & Weinberg, D. H. 1999, *ApJ*, 511, 521
- Dickinson, M., Papovich, C., Ferguson, H., & Budavári, T. 2003a, *ApJ*, 587, 25
- Dickinson, M., Stern, D., Giavalisco, M., Ferguson, H. C., Tsvetanov, Z., Chornock, R., Cristiani, S., Dawson, S., Dey, A., Filippenko, A. V., Moustakas, L. A., Nonino, M., Papovich, C., Ravindranath, S., Riess, A., Rosati, P., Spinrad, H., Vanzella, E., et al. 2003b, *ApJ*, 600, L99
- Eisenstein, D. J. & Hut, P. 1998, *ApJ*, 498, 137
- Elston, R., Rieke, G. H., & Rieke, M. 1988, *ApJ*, 331, L77
- Fan, X., Strauss, M. A., Schneider, D. P., Gunn, J. E., Lupton, R. H., Becker, R. H., Davis, M., Newman, J. A., Richards, G. T., Gordon, R. L., White, R. L., et al. 2001, *AJ*, 121, 54
- Fontana, A., Donnarumma, I., Vanzella, E., Giallongo, E., Menci, N., Nonino, M., Saracco, P., Cristiani, S., D’Odorico, S., Poli, F., et al. 2003, *ApJ*, 594, L9
- Franx, M., Labbe, I., Rudnick, G., van Dokkum, P. G., Daddi, E., Förster, S., Natascha, M., Moorwood, A., Rix, H.-W., Röttgering, H., van de Wel, A., et al. 2003, *ApJ*, 587, L79
- Furlanetto, S. R., Hernquist, L., & Zaldarriaga, M. 2004e, *MNRAS*, in press (astro-ph/0406131)
- Furlanetto, S. R., Schaye, J., Springel, V., & Hernquist, L. 2003, *ApJ*, 599, L1
- . 2004d, *ApJ*, 606, 221
- Furlanetto, S. R., Sokasian, A., & Hernquist, L. 2004a, *MNRAS*, 347, 187
- Furlanetto, S. R., Zaldarriaga, M., & Hernquist, L. 2004b, *ApJ*, in press (astro-ph/0404112)
- . 2004c, *ApJ*, in press (astro-ph/0403697)
- Glazebrook, K., Abraham, R., McCarthy, P., Savaglio, S., Chen, H.-W., Crampton, D., Murowinski, R., Jorgensen, I., Roth, K., Hook, I., Marzke, R., & Carlberg, R. 2004, *Nature*, in press (astro-ph/0401037)

- Gnedin, N. Y. 1995, *ApJS*, 97, 231
- Granato, G. L., Lacey, C. G., Silva, L., Bressan, A., Baugh, C. M., Cole, S., & Frenk, C. S. 2000, *ApJ*, 542, 710
- Hernquist, L. 1993, *ApJ*, 404, 717
- Hernquist, L. & Springel, V. 2003, *MNRAS*, 341, 1253
- Hu, E. M., McMahon, R. G., & Cowie, L. L. 1999, *ApJ*, 522, L9
- Hu, E. M. & Ridgway, S. E. 1994, *AJ*, 107, 1303
- Iwata, I., Ohta, K., Tamura, N., Ando, M., Wada, S., Watanabe, C., Akiyama, M., & Aoki, K. 2003, *PASJ*, 55, 415
- Katz, N., Weinberg, D. H., & Hernquist, L. 1996, *ApJS*, 105, 19
- Kennicutt, R. C. J. 1998, *ApJ*, 498, 541
- Kodaira, K., Taniguchi, Y., Kashikawa, N., Kaifu, N., Ando, H., Karoji, H., Ajiki, M., Akiyama, M., Aoki, K., Doi, M., et al. 2003, *PASJ*, 55, L17
- Kroupa, P. 2001, *MNRAS*, 322, 231
- Lilly, S. J., Fèvre, O. L., Hammer, F., & Crampton, D. 1996, *ApJ*, 460, L1
- Madau, P. 1995, *ApJ*, 441, 18
- McCarthy, P. J., Persson, S. E., & West, S. C. 1992, *ApJ*, 386, 52
- Menci, N., Cavaliere, A., Fontana, A., Giallongo, E., & Poli, F. 2002, *ApJ*, 575, 18
- Nagamine, K. 2002, *ApJ*, 564, 73
- Nagamine, K., Cen, R., Hernquist, L., Ostriker, J. P., & Springel, V. 2004a, *ApJ*, 610, 45
- Nagamine, K., Fukugita, M., Cen, R., & Ostriker, J. P. 2001a, *ApJ*, 558, 497
- . 2001b, *MNRAS*, 327, L10
- Nagamine, K., Springel, V., & Hernquist, L. 2004a, *MNRAS*, 348, 421
- . 2004b, *MNRAS*, 348, 435
- Nagamine, K., Springel, V., Hernquist, L., & Machacek, M. 2004b, *MNRAS*, 350, 385

- Neyrinck, M. C., Gnedin, N. Y., & Hamilton, A. J. S. 2004, MNRAS, accepted (astro-ph/0402346)
- Omont, A., Beelen, A., Bertoldi, F., & others et al. 2003, A&A, 398, 857
- Ouchi, M., Shimasaku, K., Furusawa, H., Miyazaki, M., Doi, M., Hamabe, M., Hayashino, T., Kimura, M., Kodaira, K., Komiyama, Y., et al. 2003a, ApJ, 582, 60
- . 2003b, ApJ, submitted (astro-ph/0309655)
- Pascarelle, S. M., Lanzetta, K. M., & Fernandez-Soto, A. 1998, ApJ, 508, L1
- Pei, Y. C. 1995, ApJ, 438, 623
- Poli, F., Giallongo, E., Fontana, A., Menci, N., Zamorani, G., Nonino, M., Saracco, P., Vanzella, E., Donnarumma, I., Salimbeni, S., et al. 2003, ApJ, 593, L1
- Quinn, T., Katz, N., & Efstathiou, G. 1996, MNRAS, 278, 49
- Rhoads, J. E. & Malhotra, S. 2001, ApJ, 563, L5
- Robertson, B. E., Yoshida, N., Springel, V., & Hernquist, L. 2004, ApJ, 606, 32
- Rudnick, G., Rix, H.-W., Franx, M., Labbe, I., Blanton, M., Daddi, E., Förster, S., Natascha, M., Moorwood, A., Röttgering, H., Trujillo, I., et al. 2003, ApJ, 599, 847
- Ryu, D., Ostriker, J. P., Kang, H., & Cen, R. 1993, ApJ, 414, 1
- Sawicki, M. J., Lin, H., & Yee, H. K. C. 1997, AJ, 113, 1
- Schmidt, M. 1968, ApJ, 151, 393
- Schmidt, M., Schneider, D. P., & Gunn, J. E. 1995, AJ, 110, 68
- Shapley, A. E., Steidel, C. C., Adelberger, K. L., Dickinson, M., Giavalisco, M., & Pettini, M. 2001, ApJ, 562, 95
- Smail, I., Ivison, R. J., & Blain, A. W. 1997, ApJ, 490, L5
- Smail, I., Owen, F. N., Morrison, G. E., Keel, W. C., Ivison, R. J., & Ledlow, M. J. 2002, ApJ, 581, 844
- Somerville, R. S., Primack, J. R., & Faber, S. M. 2001, MNRAS, 320, 504
- Spergel, D., Verde, L., Peiris, H. V., Komatsu, E., Nolta, M. R., Bennett, C. L., Halpern, M., Hinshaw, G., Jarosik, N., Kogut, A., et al. 2003, ApJS, 148, 175

- Springel, V. & Hernquist, L. 2002, MNRAS, 333, 649
- . 2003a, MNRAS, 339, 289
- . 2003b, MNRAS, 339, 312
- Springel, V., Tormen, G., Kauffmann, G., Yoshida, N., & White, S. D. M. 2001a, MNRAS, 328, 726
- Springel, V., Yoshida, N., & White, S. D. M. 2001b, *New Astronomy*, 6, 79
- Steidel, C. C., Adelberger, K. L., Adelberger, K. L., Shapley, A. E., Pettini, M., Dickinson, M., & Giavalisco, M. 2003, ApJ, 592, 728
- Steidel, C. C., Adelberger, K. L., Giavalisco, M., Dickinson, M., & Pettini, M. 1999, ApJ, 519, 1
- Steidel, C. C. & Hamilton, D. 1993, AJ, 105, 2017
- Steidel, C. C., Shapley, A. E., Pettini, M., Adelberger, K. L., Erb, D. K., Reddy, N. A., & Hunt, M. P. 2004, ApJ, 604, 534
- Taniguchi, Y., Ajiki, M., Murayama, T., Nagao, T., Veilleux, S., Sanders, D. B., Komiyama, Y., Shioya, Y., Fujita, S., Kakazu, Y., et al. 2003, ApJ, 585, L97
- Thoul, A. A. & Weinberg, D. H. 1996, ApJ, 465, 608
- Treyer, M. A., Ellis, R. S., Millard, B., Donas, J., & Bridges, T. J. 1998, MNRAS, 300, 303
- van Dokkum, P., Franx, M., Schreiber, N. F., Illingworth, G., Daddi, E., Knudsen, K. K., Labbe, I., Moorwood, A., Rix, H.-W., Rottgering, H., Rudnick, G., Trujillo, I., van der Werf, P., van der Wel, A., van Starckenburg, L., & Wuyts, S. 2004, ApJ, in press (astro-ph/0404471)
- Zaldarriaga, M., Furlanetto, S. R., & Hernquist, L. 2004, ApJ, in press (astro-ph/0311514)

Table 1. Simulations

| Run                       | $L_{\text{box}} [h^{-1} \text{Mpc}]$ | $N_{\text{mesh/ptcl}}$ | $m_{\text{DM}} [h^{-1} M_{\odot}]$ | $m_{\text{gas}} [h^{-1} M_{\odot}]$ | $\Delta \ell [h^{-1} \text{kpc}]$ |
|---------------------------|--------------------------------------|------------------------|------------------------------------|-------------------------------------|-----------------------------------|
| TVD: N864L22 <sup>a</sup> | 22.0                                 | 864 <sup>3</sup>       | $8.9 \times 10^6$                  | $2.2 \times 10^5$                   | 25.5                              |
| SPH: D5 <sup>b</sup>      | 33.75                                | 324 <sup>3</sup>       | $8.2 \times 10^7$                  | $1.3 \times 10^7$                   | 4.2                               |
| SPH: G6 <sup>b</sup>      | 100.0                                | 486 <sup>3</sup>       | $6.3 \times 10^8$                  | $9.7 \times 10^7$                   | 5.3                               |

Note. — Parameters of the primary simulations on which this study is based. The quantities listed are as follows:  $L_{\text{box}}$  is the simulation box size,  $N_{\text{mesh/ptcl}}$  is the number of the hydrodynamic mesh points for TVD or the number of gas particles for SPH,  $m_{\text{DM}}$  is the dark matter particle mass,  $m_{\text{gas}}$  is the mass of the baryonic fluid elements in a grid cell for TVD or the masses of the gas particles in the SPH simulations. Note that TVD uses  $432^3$  dark matter particles for N864 runs.  $\Delta \ell$  is the size of the resolution element (cell size in TVD and gravitational softening length in SPH in comoving coordinates; for proper distances, divide by  $1 + z$ ). The upper indices on the run names correspond to the following sets of cosmological parameters:  $(\Omega_{\text{M}}, \Omega_{\Lambda}, \Omega_b, h, n, \sigma_8) = (0.29, 0.71, 0.047, 0.7, 1.0, 0.85)$  for (a), and  $(0.3, 0.7, 0.04, 0.7, 1.0, 0.9)$  for (b).



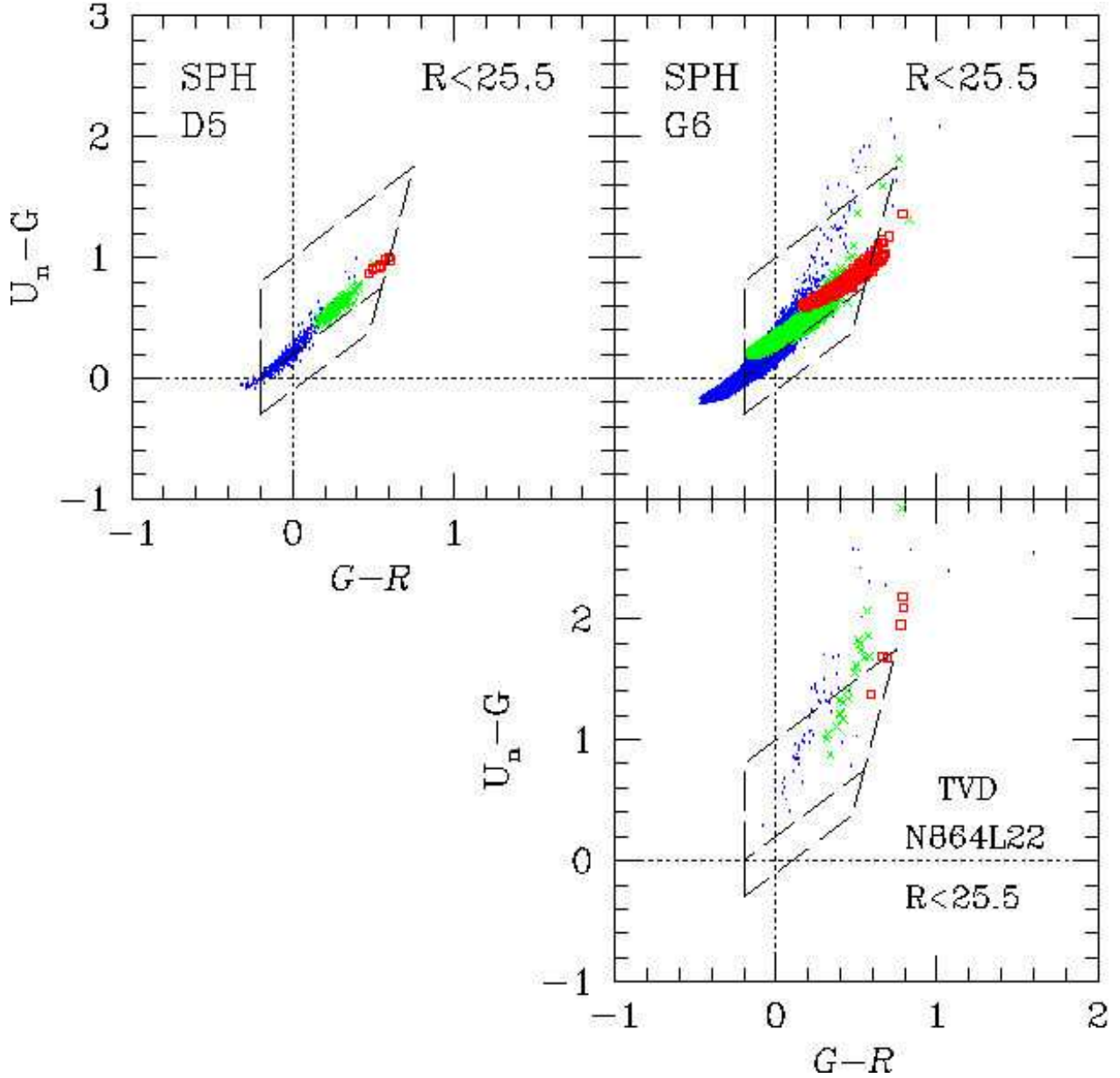


Fig. 1.— Color-color diagrams of simulated galaxies at  $z = 2$  in the observed-frame  $U_n - G$  vs.  $G - R$  plane for both SPH (top 2 panels) and TVD (bottom right panel) simulations. Only those galaxies that are brighter than  $R = 25.5$  are shown to match the magnitude limit of the Steidel et al. (2004) sample. The three different symbols represent three different values of Calzetti extinction:  $E(B - V) = 0.0$  (blue dots),  $0.15$  (green crosses), and  $0.3$  (red open squares). The number density of galaxies shown (i.e.  $R < 25.5$ ) is given in the bottom right corner of each panel for  $E(B - V) = 0.0, 0.15, 0.30$  from top to bottom, respectively. The color-selection criteria used by Adelberger et al. (2004) and Steidel et al. (2004) are shown by the long-dashed boxes. The upper (lower) box corresponds to their BX (BM) criteria for selecting out galaxies at  $z = 2.0 - 2.5$  ( $z = 1.5 - 2.0$ ).

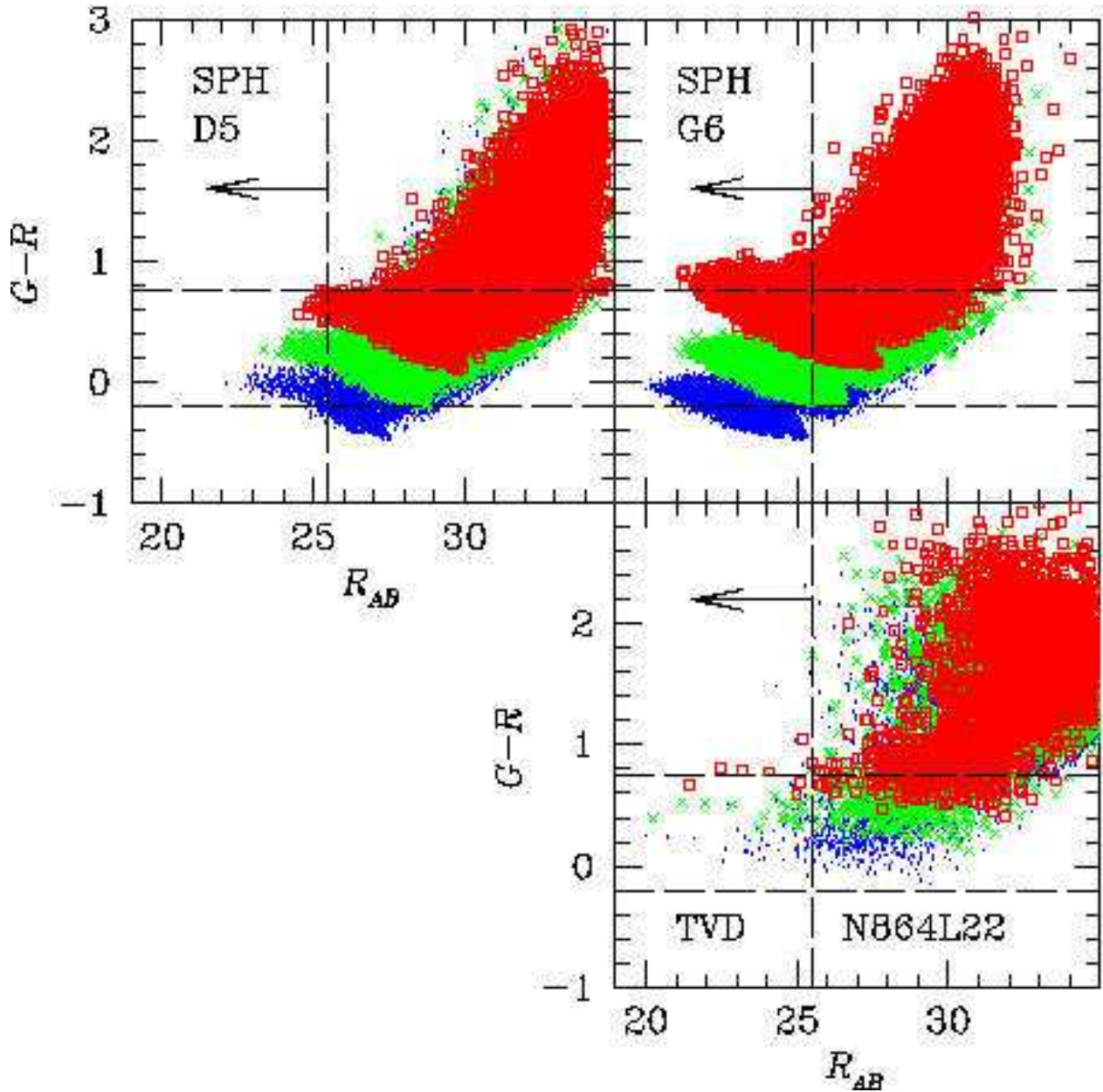


Fig. 2.— Color-magnitude diagrams of simulated galaxies at  $z = 2$  on the  $R$  vs.  $G - R$  plane for both SPH (top 2 panels) and TVD (bottom right panel) simulations. All simulated galaxies are shown. Blue dots, green crosses, and red open squares correspond to  $E(B - V) = 0.0, 0.15, 0.30$ . The magnitude limit of  $R = 25.5$  and the color range of  $-0.2 < G - R < 0.75$  used by Steidel et al. (2004) and Adelberger et al. (2004) are shown by the long-dashed lines.

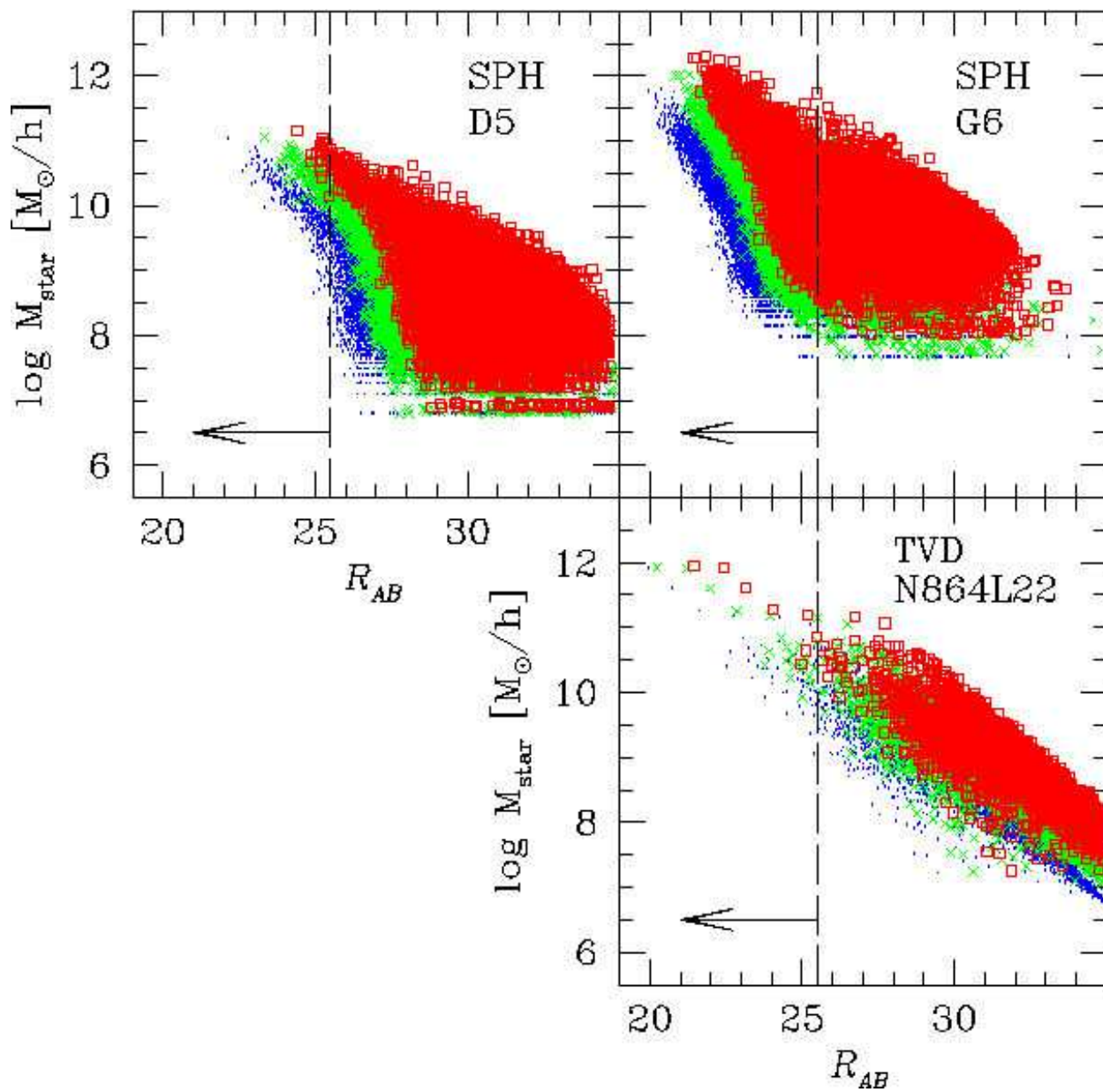


Fig. 3.— Observed-frame  $R$  magnitude vs. stellar masses of simulated galaxies at  $z = 2$  for both SPH (top 2 panels) and TVD (bottom right panel) simulations. Blue dots, green crosses, and red open squares correspond to  $E(B - V) = 0.0, 0.15, 0.30$ . The magnitude limit of  $R = 25.5$  used by Steidel et al. (2004) is shown by the vertical long-dashed line.

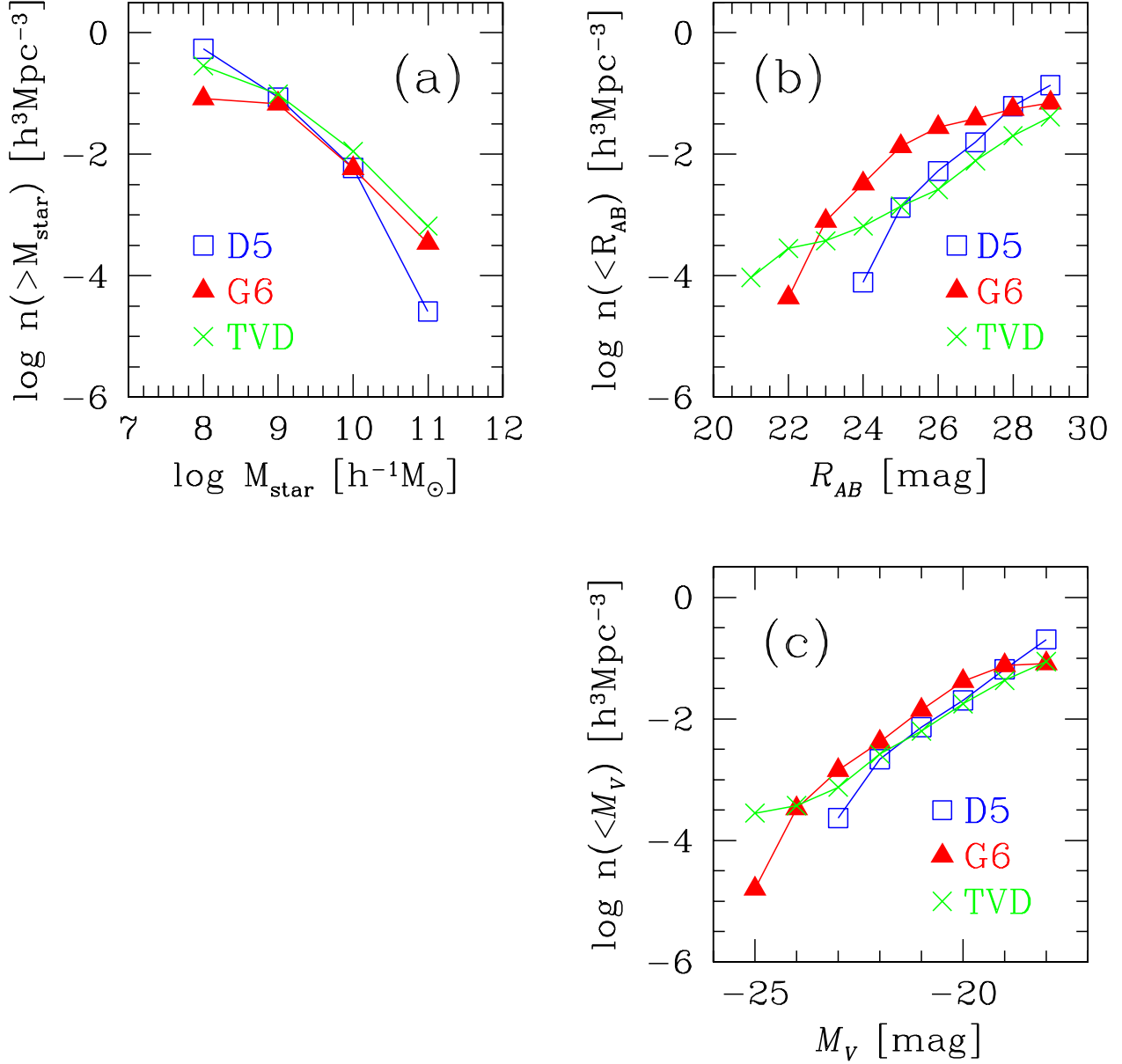


Fig. 4.— Number density of all galaxies with stellar mass [*panel (a)*], observed-frame *R*-band magnitude [*panel (b)*], rest-frame *V*-band magnitude [*panel (c)*] above a certain value on the abscissa. The symbols correspond to the results from the SPH D5 run (blue open squares), the G6 run (red filled triangles), and the TVD run (green crosses).

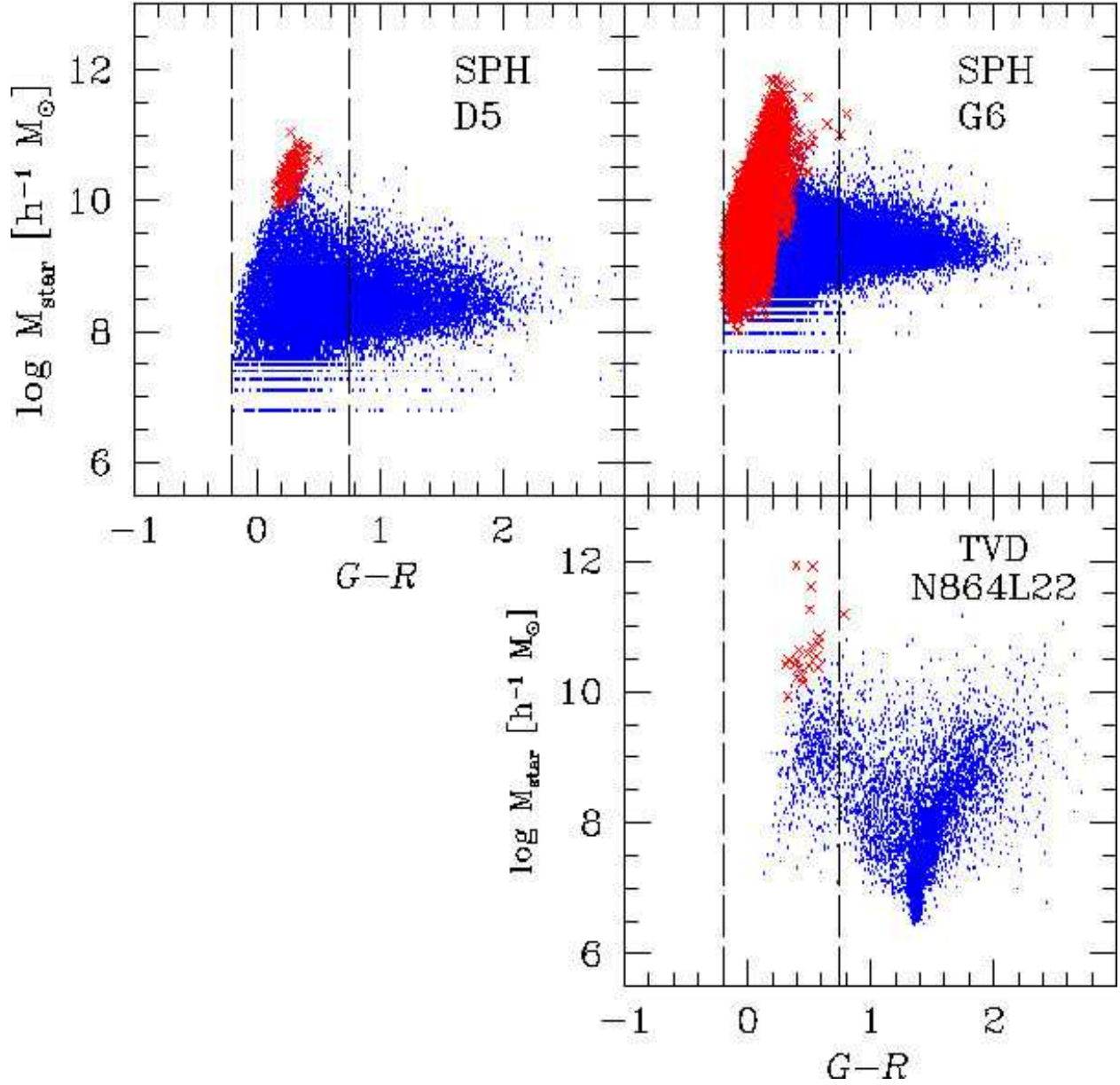


Fig. 5.— Stellar masses vs.  $G - R$  color of simulated galaxies at  $z = 2$  in the observed-frame for both SPH (top 2 panels) and TVD (bottom right panel) simulations. The red open crosses show the galaxies that are brighter than  $R = 25.5$ , while the remainder of the points are shown in blue dots. Here, only the case for  $E(B - V) = 0.15$  is shown. The most massive galaxies are not the bluest ones owing to the underlying old stellar population. The color range of  $-0.2 < G - R < 0.75$ , which is the  $G - R$  color range of the selection criteria shown in Figure 1, is indicated by the vertical long-dashed lines.

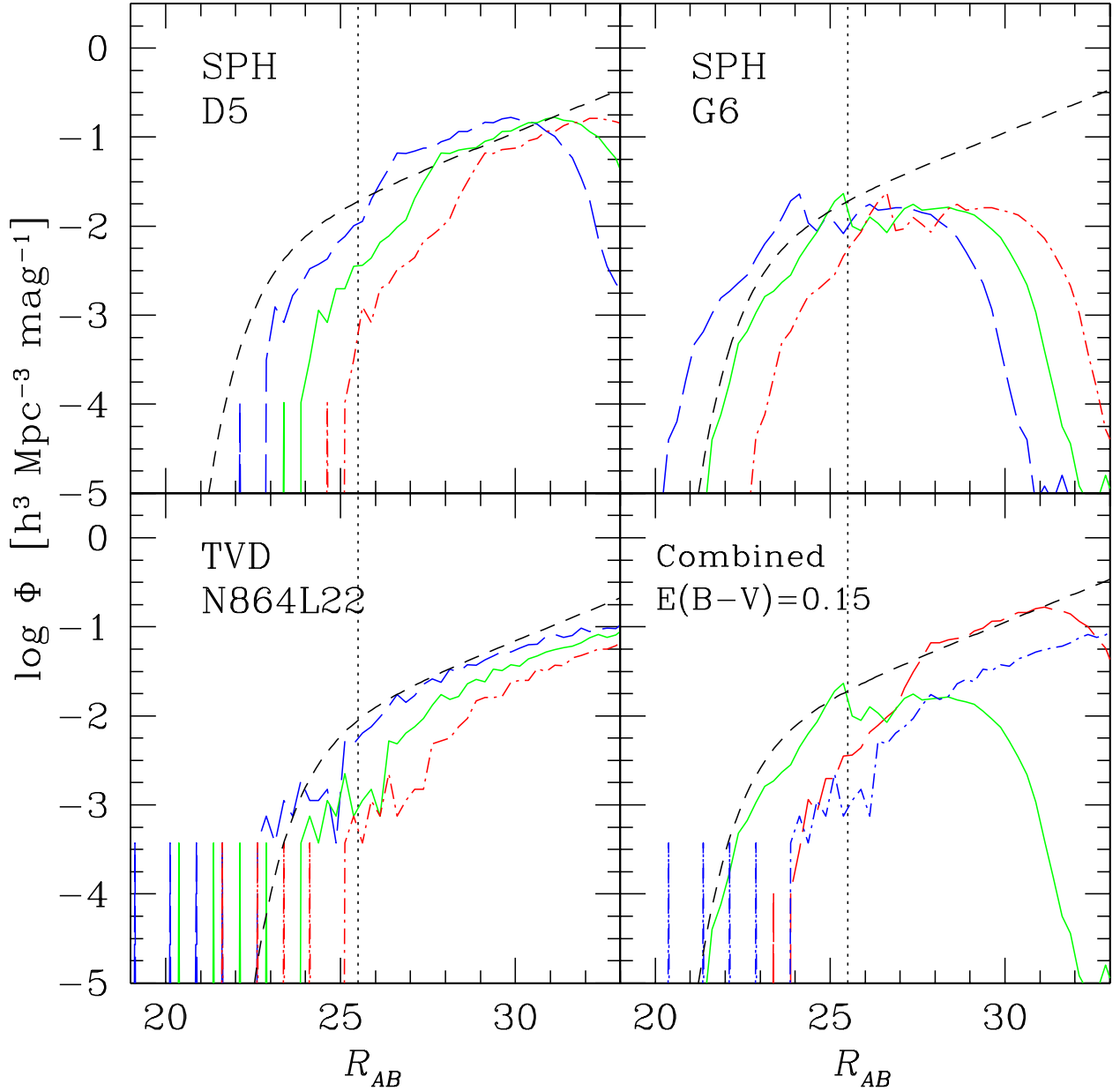


Fig. 6.—  $R$  band luminosity function in the observed-frame for all simulated galaxies at  $z = 2$  for both SPH (top 2 panels) and TVD (bottom left panel) simulations. For these 3 panels, blue long-dashed, green solid, and red dot-short-dashed lines correspond to  $E(B - V) = 0.0, 0.15, 0.30$ , respectively. The vertical dotted line indicates the magnitude limit of  $R = 25.5$  used by Steidel et al. (2004). In the bottom right panel, a combined result is shown with the SPH D5 (green solid line), G6 (red long-dashed), and TVD (blue dot-dashed) results overplotted for the case of  $E(B - V) = 0.15$ . For comparison, the Schechter functions with following parameters are shown in short-dashed lines:  $(\Phi^*, M_R^*, \alpha) = (1 \times 10^{-2}, 23.2, -1.4)$  for SPH D5 & G6 (top two panels), and combined results (bottom right panel), and  $(1 \times 10^{-2}, 24.5, -1.4)$  for the TVD run (bottom left panel), respectively.

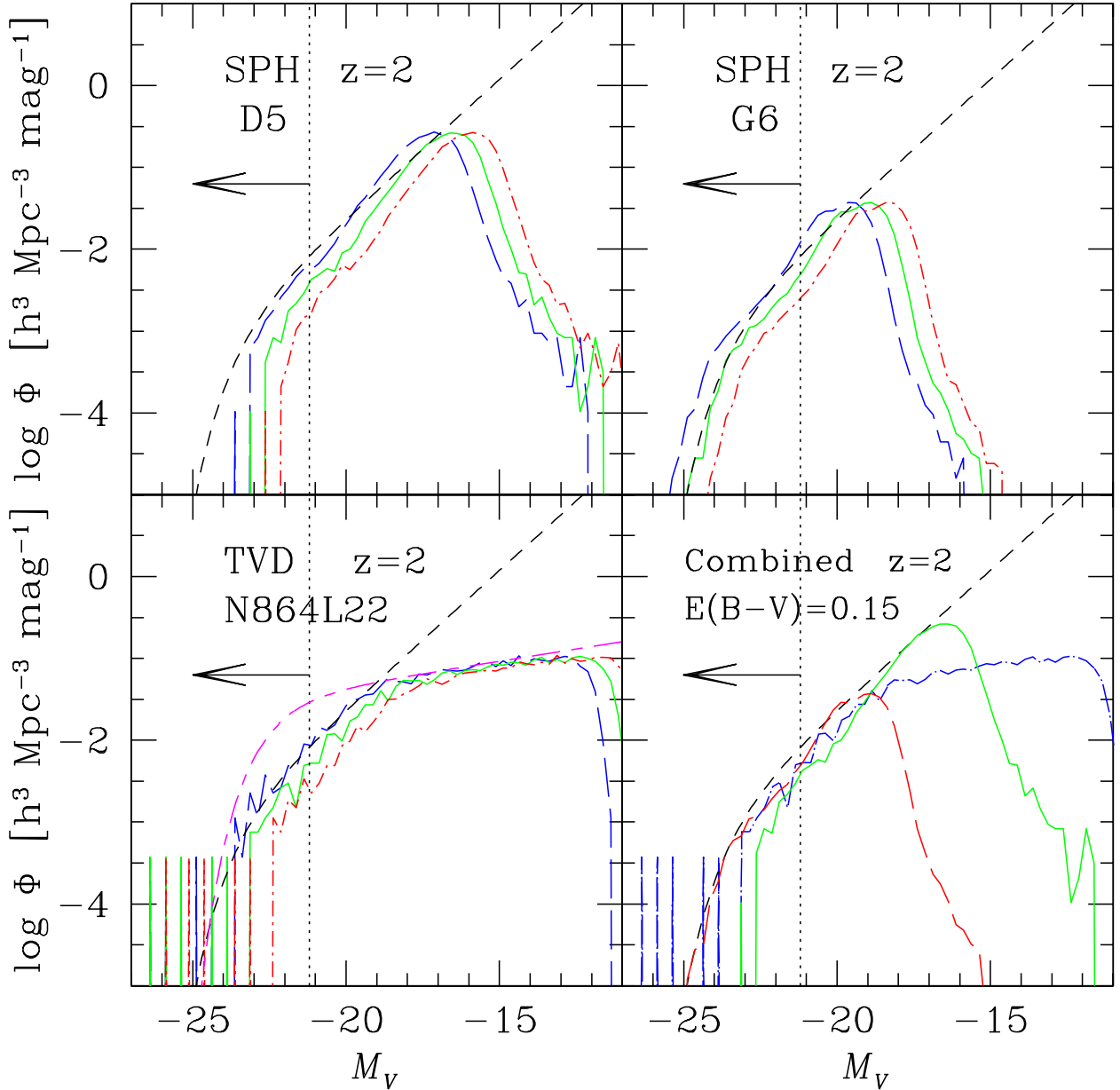


Fig. 7.— Rest-frame  $V$ -band luminosity function of all simulated galaxies at  $z = 2$  for both SPH (top 2 panels) and TVD (bottom left panel) simulations. For these 3 panels, blue long-dashed, green solid, and red dot-short-dashed lines correspond to  $E(B - V) = 0.0, 0.15, 0.30$ , respectively. In the bottom right panel, a combined result is shown with the SPH D5 (green solid line), G6 (red long-dashed), and TVD (blue dot-dashed) results overplotted for the case of  $E(B - V) = 0.15$ . The magnitude limit of  $M_V = -21.2$  (for  $h = 0.7$ ) for the survey of the LBGs at  $z = 3$  by Shapley et al. (2001) is shown by the vertical dotted line. To guide the eye, a Schechter function with parameters  $(\Phi^*, M_V^*, \alpha) = (1.8 \times 10^{-3}, -23.4, -1.8)$  is shown in the short-dashed curve in all panels. In the bottom left panel of TVD run, another Schechter function with parameters  $(\Phi^*, M_V^*, \alpha) = (3.5 \times 10^{-2}, -22.5, -1.15)$  is also shown as a magenta long-dash-short-dashed line.

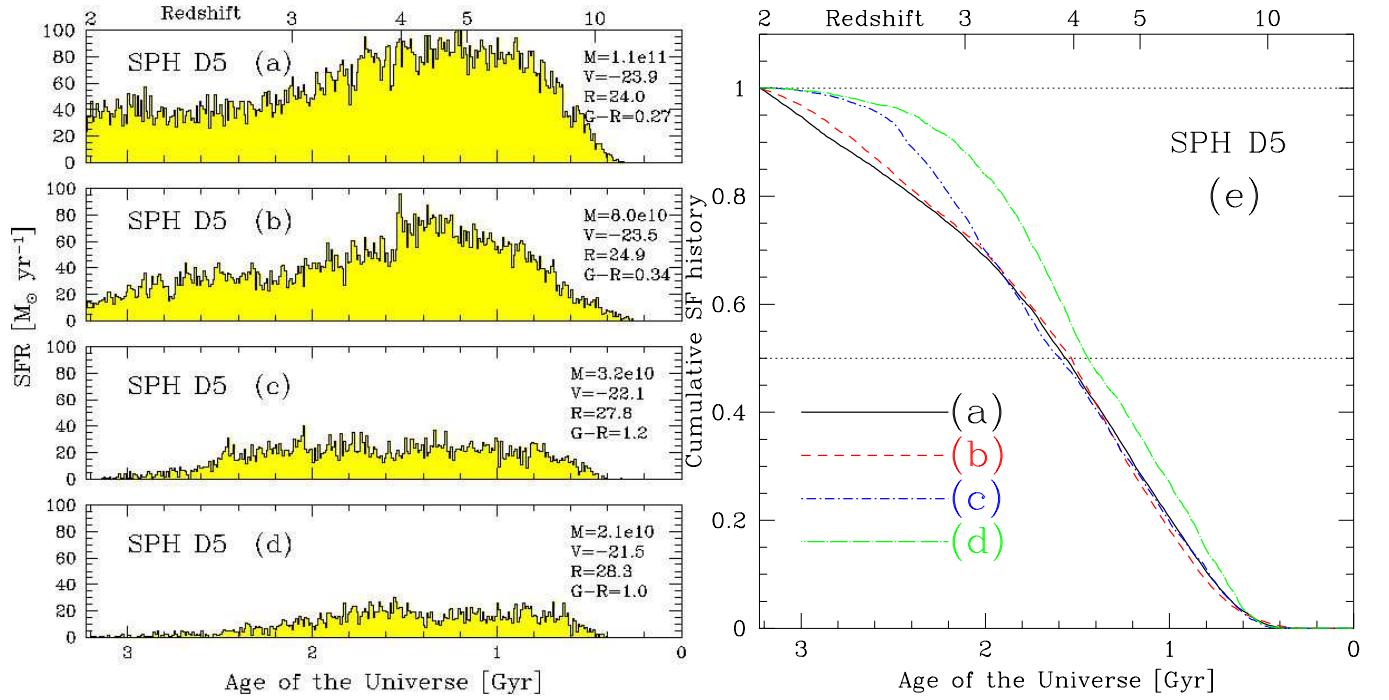


Fig. 8.— *Panels (a) - (d)*: Star formation history as a function of cosmic time for selected galaxies in the SPH D5 run. In the right side of panels (a) – (d), the following values for the case of  $E(B - V) = 0.15$  are listed: stellar mass in units of  $h^{-1}M_{\odot}$ , rest-frame V-band magnitude, observed-frame  $R$ -band magnitude, and  $G - R$  color. Galaxies (a) & (b) are the two most massive galaxies, and (c) & (d) are the two reddest galaxies with  $M_{\text{star}} > 1 \times 10^{10} h^{-1} M_{\odot}$ . *Panel (e)*: Cumulative SF history of galaxies (a) - (d).



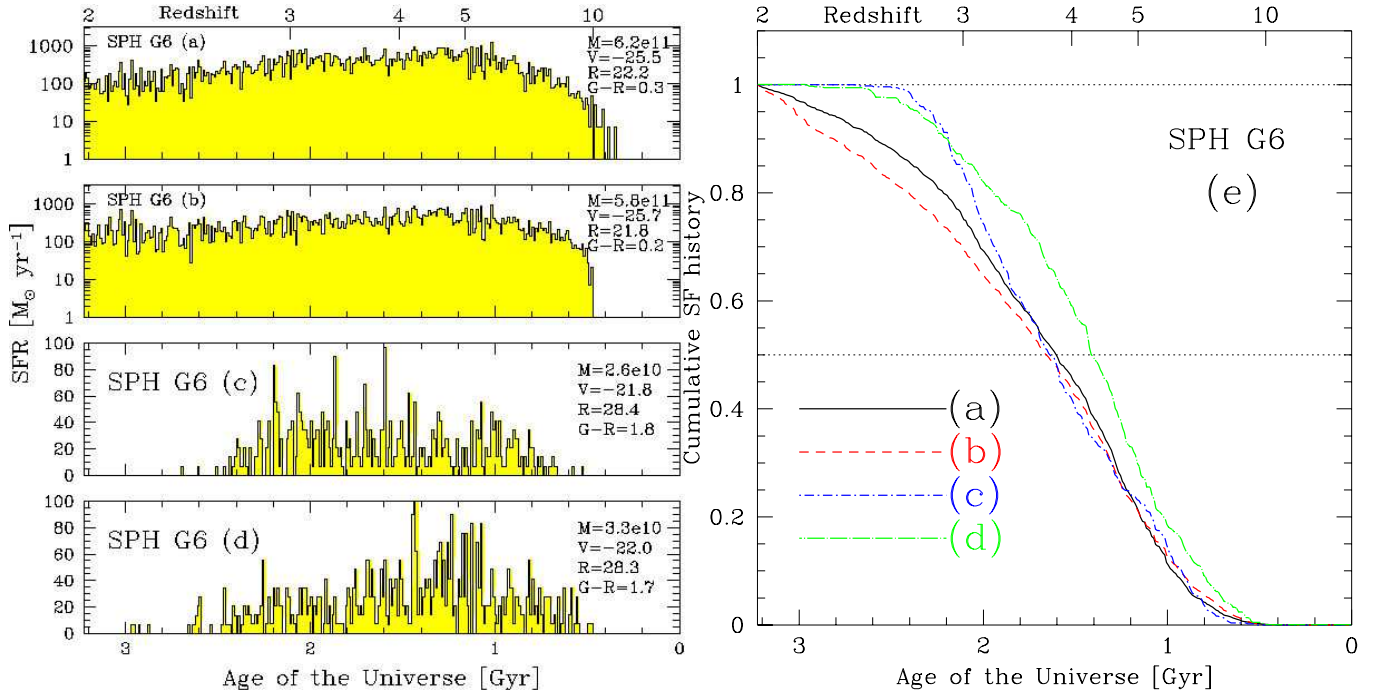


Fig. 9.— *Panels (a)-(d)*: Star formation history as a function of cosmic time for selected galaxies in the SPH G6 run. In the right side of each panel, the following values are listed: stellar mass in units of  $h^{-1}M_{\odot}$ , rest-frame V-band magnitude, observed-frame  $R$ -band magnitude, and  $G - R$  color. Galaxies (a) & (b) are the two most massive galaxies, and (c) & (d) are the two reddest galaxies with  $M_{\text{star}} > 1 \times 10^{10} h^{-1} M_{\odot}$ . Note that panels (a) & (b) use a logarithmic scale for the ordinate, while panels (c) & (d) use a linear scale. *Panel (e)*: Cumulative SF history of galaxies (a) - (d).

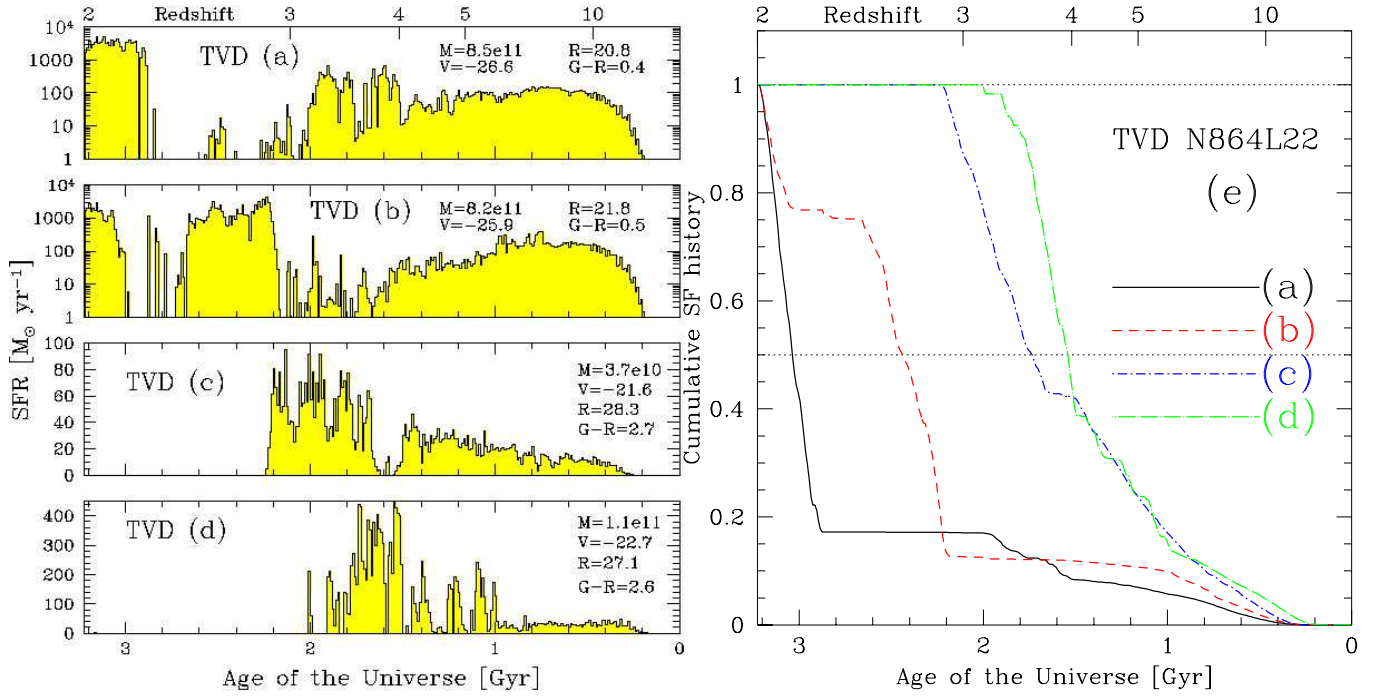


Fig. 10.— *Panels (a)-(d)*: Star formation history as a function of cosmic time for selected galaxies in the TVD N864L22 run. In each panel, the following values are listed: stellar mass in units of  $h^{-1}M_{\odot}$ , rest-frame V-band magnitude, observed-frame  $R$ -band magnitude, and  $G-R$  color. Galaxies (a) & (b) are the two most massive galaxies, and (c) & (d) are the two reddest galaxies with  $M_{\text{star}} > 1 \times 10^{10} h^{-1} M_{\odot}$ . Note that panels (a) & (b) use a logarithmic scale for the ordinate, while panels (c) & (d) use a linear scale. *Panel (e)*: Cumulative SF history of galaxies (a) - (d).

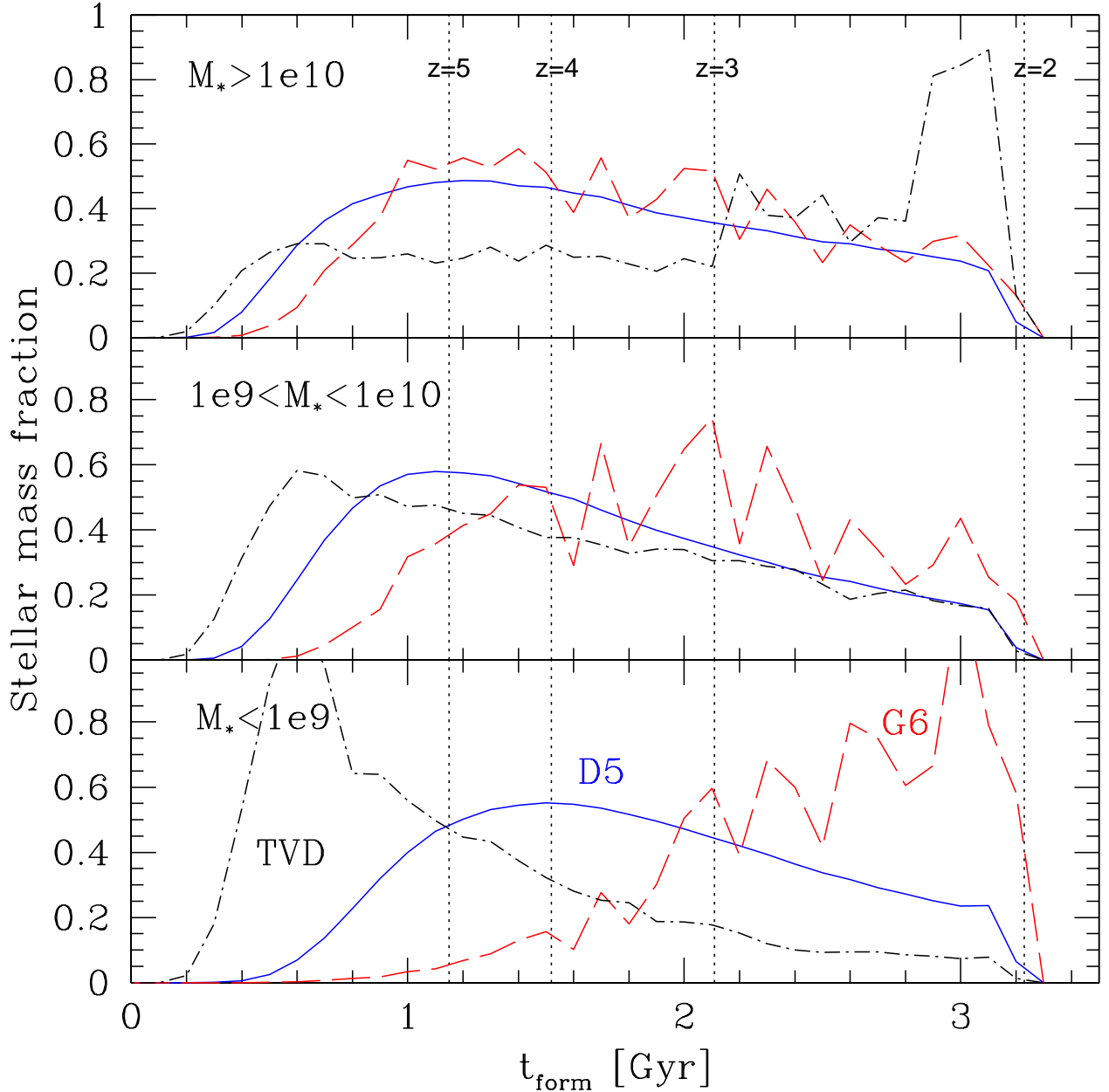


Fig. 11.— Distribution of stellar masses in the simulations as a function of formation time ( $t_{\text{form}} = 0$  corresponds to the Big Bang). The galaxy sample is divided into 3 categories by their stellar mass:  $M_{\text{star}} > 10^{10}h^{-1}M_{\odot}$  (top panel),  $10^9 < M_{\text{star}} < 10^{10}h^{-1}M_{\odot}$  (middle panel),  $M_{\text{star}} < 10^9h^{-1}M_{\odot}$  (bottom panel). Different line types correspond to different simulations: red long-dashed (SPH G6 run), blue solid (SPH D5 run), and black dot-dashed (TVD N864L22 run). The vertical dotted lines indicate four epochs of  $z = 2, 3, 4,$  &  $5$ , as indicated in the top panel.